Article

Cell Systems

Asymmetric Damage Segregation Constitutes an Emergent Population-Level Stress Response

Graphical Abstract

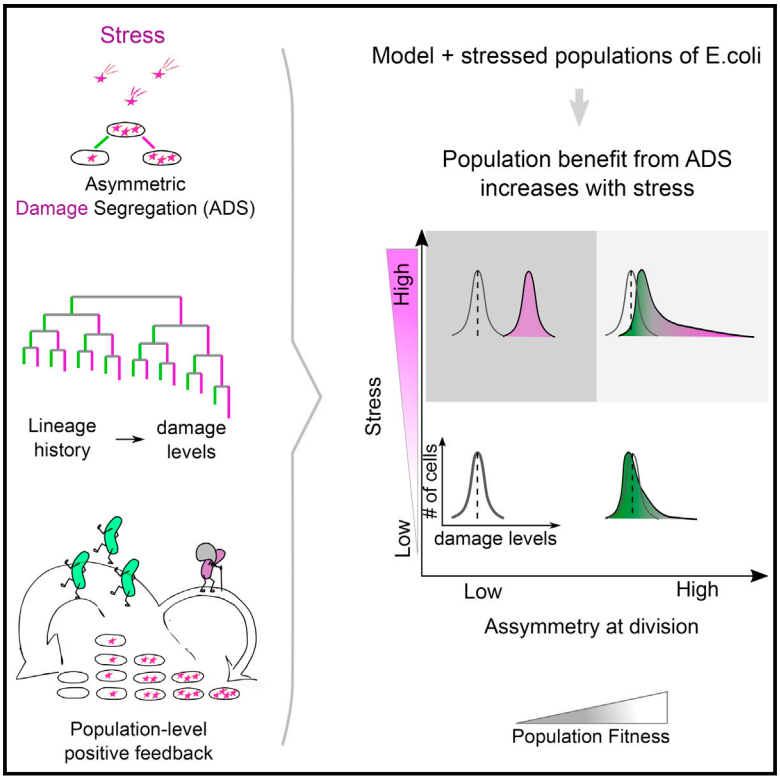

Highlights

- Lineages and growth rate distributions reveal effects of ADS
- Asymmetry of segregation is dependent on single-cell damage
- The population benefit of ADS increases with stress

Authors

Søren Vedel, Harry Nunns, Andrej Košmrlj, Szabolcs Semsey, Ala Trusina

Correspondence

svedel@nbi.ku.dk (S.V.),
trusina@nbi.ku.dk (A.T.)

In Brief

Asymmetric damage segregation (ADS) is non-random, asymmetric partitioning of damage at cell division. Using theory and time-lapse imaging of *E. coli* colonies, we find that the extent of ADS increases with severity of stress through a combination of single-cell and population-level feedbacks.

Vedel et al., 2016, Cell Systems *3*, 187–198
August 24, 2016
http://dx.doi.org/10.1016/j.cels.2016.06.008

Cell Systems
Article

Asymmetric Damage Segregation Constitutes an Emergent Population-Level Stress Response

Søren Vedel,[1,2,*] Harry Nunns,[1,3] Andrej Košmrlj,[4] Szabolcs Semsey,[1] and Ala Trusina[1,*]
[1]Center for Models of Life
[2]Niels Bohr International Academy
Niels Bohr Institute, University of Copenhagen, Blegdamsvej 17, 2100 Copenhagen, Denmark
[3]Division of Biology and Biological Engineering, California Institute of Technology, 1200 E. California Boulevard, Pasadena, CA 91125, USA
[4]Department of Mechanical and Aerospace Engineering, Princeton University, Princeton, NJ 08544, USA
*Correspondence: svedel@nbi.ku.dk (S.V.), trusina@nbi.ku.dk (A.T.)
http://dx.doi.org/10.1016/j.cels.2016.06.008

SUMMARY

Asymmetric damage segregation (ADS) is a mechanism for increasing population fitness through non-random, asymmetric partitioning of damaged macromolecules at cell division. ADS has been reported across multiple organisms, though the measured effects on fitness of individuals are often small. Here, we introduce a cell-lineage-based framework that quantifies the population-wide effects of ADS and then verify our results experimentally in *E. coli* under heat and antibiotic stress. Using an experimentally validated mathematical model, we find that the beneficial effect of ADS increases with stress. In effect, low-damage subpopulations divide faster and amplify within the population acting like a positive feedback loop whose strength scales with stress. Analysis of protein aggregates shows that the degree of asymmetric inheritance is damage dependent in single cells. Together our results indicate that, despite small effects in single cell, ADS exerts a strong beneficial effect on the population level and arises from the redistribution of damage within a population, through both single-cell and population-level feedback.

INTRODUCTION

To cope with unfavorable environmental conditions, cells have evolved myriad strategies that operate on both the single-cell and population level. As a first line of defense, cells use versatile cellular repair mechanisms to counteract macromolecular damage caused by environmental stress. However, the repair is not perfect and may not prevent accumulation of DNA mutations or protein aggregates within single cells. To accommodate this, additional stress responses operate at the population level within populations of genetically identical individuals. In particular, during cellular division in bacteria (Winkler et al., 2010; Stewart et al., 2005), yeasts (Coelho et al., 2013; Aguilaniu et al., 2003; Zhou et al., 2011; Liu et al., 2011), and stem cells (Fuentealba et al., 2008; Bufalino et al., 2013; Rujano et al., 2006), accumulated damage is unequally allotted to the two resulting cells. This asymmetric damage segregation (ADS) produces one faster-growing "rejuvenated" cell at the cost of a more damaged, slower-growing "aged" cell. In silico models suggest that ADS increases the reproductive rate and survival of cellular populations (Chao, 2010; Ackermann et al., 2007; Erjavec et al., 2008; Watve et al., 2006) under the conditions when efficiency of repair is low compared to the rate of damage accumulation (Clegg et al., 2014). Despite these potential benefits, ADS is not an obligate response and is observed in only a fraction of cells (Yennek et al., 2014), cell types (Bufalino et al., 2013), and environments (Stewart et al., 2005; Wang et al., 2010; Coelho et al., 2013; Yennek et al., 2014; Rang et al., 2012).

While the *single-cell* mechanisms underlying ADS are partially understood (Spokoini et al., 2012; Liu et al., 2011; Malinovska et al., 2012; Kaganovich et al., 2008; Specht et al., 2011; Winkler et al., 2010), it remains unclear what the key determinants are for ADS to emerge and become beneficial at the *level of the population.* To characterize the extent of asymmetry, many studies focus on pairwise comparisons of cells after division (Coelho et al., 2013; Stewart et al., 2005; Lindner et al., 2008; Winkler et al., 2010; Ackermann et al., 2007; Bufalino et al., 2013; Yennek et al., 2014). This approach may underestimate population-level effects as it relies on the assumptions that all cell pairs exhibit the same level of ADS. To our knowledge, thorough analysis of the actual population structure has been performed. Moreover, it is unknown how significant the effects of ADS are when compared to other sources of cell-to-cell heterogeneity.

Here, we address these issues using asymmetric division of protein aggregates in *Escherichia coli* as a model system. In *E. coli*, damaged proteins form aggregates throughout the cell; these localize to the older pole (pre-existing from previous division) after several cellular divisions (Lindner et al., 2008). By combining whole-population experiments—where single-cell growth and aggregate dynamics were measured for over 11,000 *E. coli* cells—with mathematical model, we find that the magnitude of ADS within a population is an emergent property that scales with the level of stress applied. The emergence is mediated by single-cell and population-level feedback loops, acting to continuously re-distribute damage within individuals and optimize population-level growth. Contrary to earlier assumptions, this comprehensive whole-population mapping reveals that the levels of ADS are not the same in all cells but are

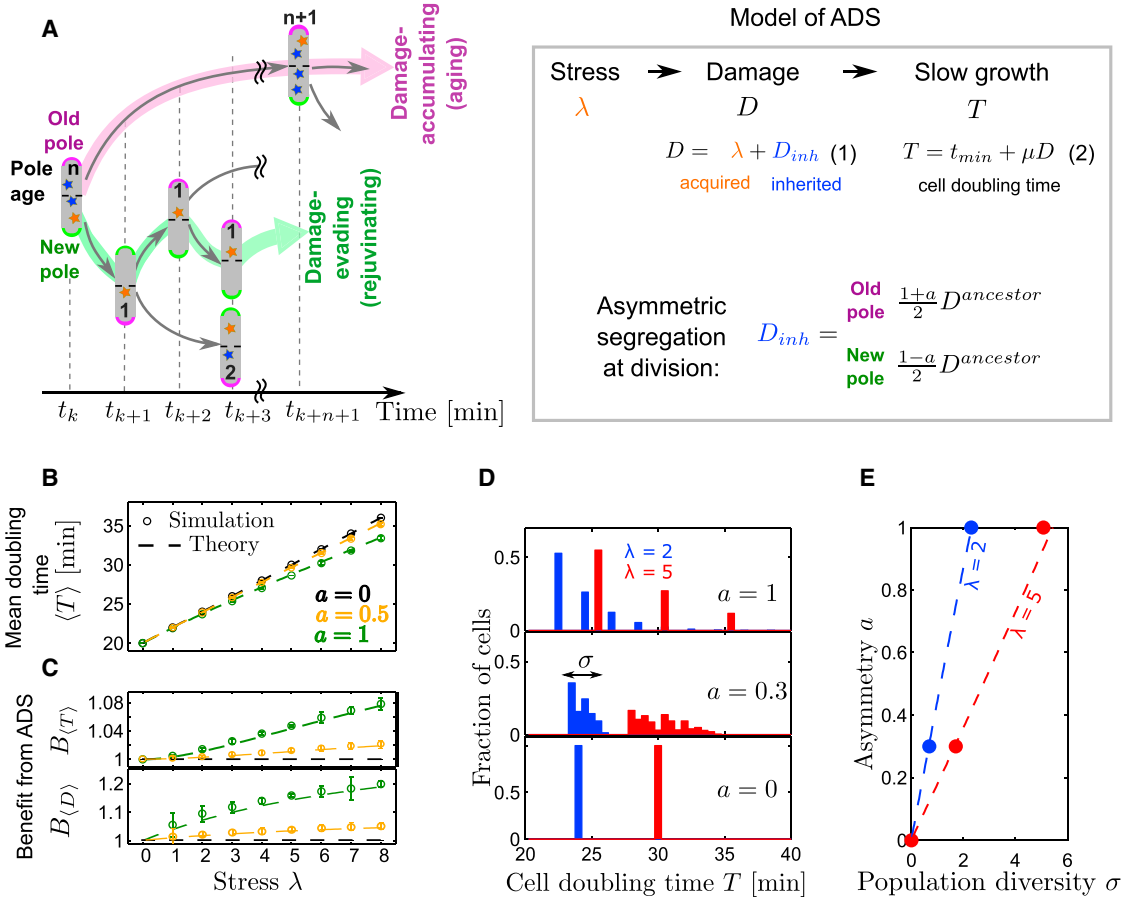

Figure 1. Model Formulation and Key Predictions

(A) Schematic of the damage segregation in a lineage-based model. Old poles are marked in magenta and new poles in green; cell pole age is measured by its number of consecutive old-pole divisions. Blue stars mark inherited damage; orange stars mark new damage acquired between two consecutive divisions. Right panel summarizes key equations of the mathematical model.

(B) Mean doubling time $\langle T \rangle$ increases with stress, λ, but decreases with asymmetry, *a*. Circles, simulation; dashed lines, theoretical expression (Equation S7). We use a stochastic simulation algorithm for computational efficiency (see Experimental Procedures), and the error bars indicate the SEM caused by the stochasticity.

(C) The population benefit *B* from ADS increases with stress and asymmetry. The benefits for doubling times, $B_{\langle T \rangle}$ and damage $B_{\langle D \rangle}$, are defined as fold decrease in mean doubling time and damage due to ADS (see Experimental Procedures). Error bars indicate the SE of the benefit due to the use of a stochastic algorithm.

(D and E) Both the asymmetry and stress affect the shape of the doubling-time distribution by increasing the cell-to-cell variability, which is quantified by distribution width, σ, in (E). Dashed lines show theoretical results of the deterministic model (Equation S8); filled circles mark the distribution widths from simulations in (D).

See also Figure S1.

determined by the cell's lineage history, such that cells with more damage exhibit a higher level of asymmetry. Finally, using lineage-based tools for ADS analysis that we introduce here, we show that measured levels of ADS indeed confer a population-level advantage even when masked by cell-to-cell variability that is unrelated to ADS.

RESULTS

Predictions of the Population Benefit from ADS Using a Lineage-Based Mathematical Model

To investigate how ADS affects population structure and dynamics, we considered a conceptually simple mathematical model of cells in growing population subject to ADS (Figure 1A). Many molecular details regarding ADS remain obscure, or cell- or damage-type specific, so we focused instead on simple mathematical implementations of general concepts relevant to ADS. While similar in silico models were investigated earlier (Ackermann et al., 2007; Erjavec et al., 2008; Chao, 2010), the effects of environmental stress nonetheless remain largely unexplored. By treating the population as a set of evolving lineages rather than a collection of individual cells (see Supplemental Information, section V), we derived analytical relationships between (1) the severity of environmental stress λ, (2) physiological properties such as doubling times *T*, damages *D*, and (3) and cell-to-cell variation σ, representing the population effects of ADS (see Figure 1 and Equations S7 and S8). Theoretical results were paralleled by numerical simulation of the model (see

Experimental Procedures and Supplemental Information, section IV).

In this model, each cell inherits a lineage-dependent amount of accumulated damage, D_{inh}, from its ancestor (Figure 1A). Over its lifetime between divisions, each cell acquires additional damage, proportional to the severity of stress λ, resulting in the total damage

$$D = D_{inh} + \lambda \qquad \text{(Equation 1)}$$

prior to division. Accumulated damage slows down cell growth (Lindner et al., 2008), so we set the doubling time T of the cell to linearly depend on its total amount of damage,

$$T = t_{min} + \mu D = t_{min} + \mu(D_{inh} + \lambda), \qquad \text{(Equation 2)}$$

where μ is a proportionality constant relating damage and time, and t_{min} is the minimum doubling time of a cell set by mechanisms unrelated to ADS. ADS is introduced into the model through an asymmetry parameter a $(0 \le a \le 1)$ that dictates the amount of damage inherited by each sister cell at division. The old-pole (magenta, Figure 1A) cell inherits a larger fraction of the ancestor's damage $D_{inh}^{old} = (1+a)/2D^{ancestor}$, while the new-pole cell inherits a fraction $D_{inh}^{new} = (1-a)/2D^{ancestor}$, resulting in a doubling-time difference between two sister cells

$$T_{old} - T_{new} = \mu a D^{ancestor}. \qquad \text{(Equation 3)}$$

This equation reveals that the difference in sister-cell doubling times is a product of both the lineage history (via $D^{ancestor}$) and single-cell behavior (via a). We initially treat the asymmetry parameter as a constant across all cells, but we will later relax this assumption. To speed up the convergence of our simulations, we have added small zero-mean noise to the cell's doubling time. Theoretical results are deterministic (see Experimental Procedures).

In line with previous in silico findings (Ackermann et al., 2007; Erjavec et al., 2008; Chao, 2010), our modeling results show that ADS reduces the mean doubling time. We find that this effect is greater under higher stress (Figures 1B and S1A). Consequently, the benefit of ADS (defined as the fold-change improvement of physiological properties at some asymmetry $(a \ge 0)$ relative to symmetry $(a = 0)$, Experimental Procedures) increases with stress and is thus *stress adaptive* (Figure 1C). We emphasize that the term "adaptive" refers to phenotypic changes in response to variations in the external environment, and not to evolutionary changes mediated by natural selection. Moreover, we find that stress also has a strong influence on population structure because of ADS (see Figure 1D). As a result of the continuous and non-random redistribution of damage at division, each cell lineage has a *unique lineage history* of damage-evasion and -accumulation events (Figure 1A). These unique lineage histories diversify the cells in the population, and our model predicts that the population diversity (characterized by width σ of the distribution of doubling times) increases with both asymmetry and stress (Figures 1E and S1B).This is likely why ADS has primarily been observed (prior to this study) under conditions of significant stress (Stewart et al., 2005; Lindner et al., 2008; Winkler et al., 2010; Coelho et al., 2013; Rang et al., 2012; Iyer-Biswas et al., 2014).

The stress-adaptive behavior of ADS stems from a positive feedback that amplifies population diversity. This feedback occurs because low-damage cells divide faster than the rest of the population (Equation 2) and at the same time gives rise to low-damage progeny. In this way, damage-evading lineages (lineages that consecutively inherit the smaller fraction of damage) become over-represented, reducing the mean doubling time. The feedback strength is related to the sister-cell difference in doubling times, ΔT, which depends on the level of environmental stress λ through the lineage damage $D^{ancestor}$ (Equation 3). Thus, the feedback is stronger (resulting in stress adaptation) under higher stress. Moreover, since the feedback strength also depends on a, higher asymmetries also lead to increased stress adaptation.

Our model reveals that this population-level stress response is an *emergent property* of a population in which two *simple rules* hold for single cells: (1) cells "interact" through asymmetric inheritance of damage (e.g., protein aggregates or mutated DNA strands) and (2) cells with lower damage have phenotypical advantage (e.g., shorter doubling time or increased number of times cell divides before senescence). Thus, we expect that this effect should emerge regardless of the exact mechanism of ADS.

Experimental Validation of Model Predictions

We tested the predictions experimentally in exponentially growing populations of *E. coli* by monitoring single-cell doubling times and protein aggregates. Constant environmental stress was imposed in the form of heat shock or antibiotic stress (kanamycin), as both are known to induce protein aggregation (Van-Bogelen and Neidhardt, 1990). To track the effects of ADS across multiple lineage histories, we monitored growing colonies starting from single cell and up to ~300 cells. Since protein aggregates are known to be the predominant factor in *E. coli* ADS (Lindner et al., 2008; Winkler et al., 2010), we expressed the heat shock chaperone ClpB fused to YFP via a medium-copy plasmid within clpB knockout cells (see Experimental Procedures and Figure 4A). This reporter allowed us to experimentally measure the asymmetry parameter a by monitoring aggregate formation and inheritance. Compared to other chaperones, ClpB showed a higher level of co-localization with aggregates, and the fusion has been shown to be functional (Winkler et al., 2010), making it an effective marker. We also verified the results of experiments with wild-type *E. coli* (all experiments are summarized in Table S1).

Lineage-Based Data Analysis Captures the Population-Level Effects of ADS

We developed a lineage-based data-analysis framework centered on binning cells with similar lineage histories to properly investigate the population structure. If the damage re-distribution is governed primarily by ADS, cells in the same bin would have similar damage levels. Variations between bins (caused by differences in accumulated damage) is therefore a signature of ADS, while within-bin variations would be caused by ADS-unrelated variations, which we refer to as noise. We approximated the full lineages by binning the cells based on the number h of consecutive events of damage accumulation (positive h) or evasion (negative h) for both the current cell and its immediate ancestor: $h_{current}$, $h_{ancestor}$ (see Experimental Procedures and Figure 2B). The median doubling time in each lineage served as our *noise-filtered readout* coupling to the lineage-specific

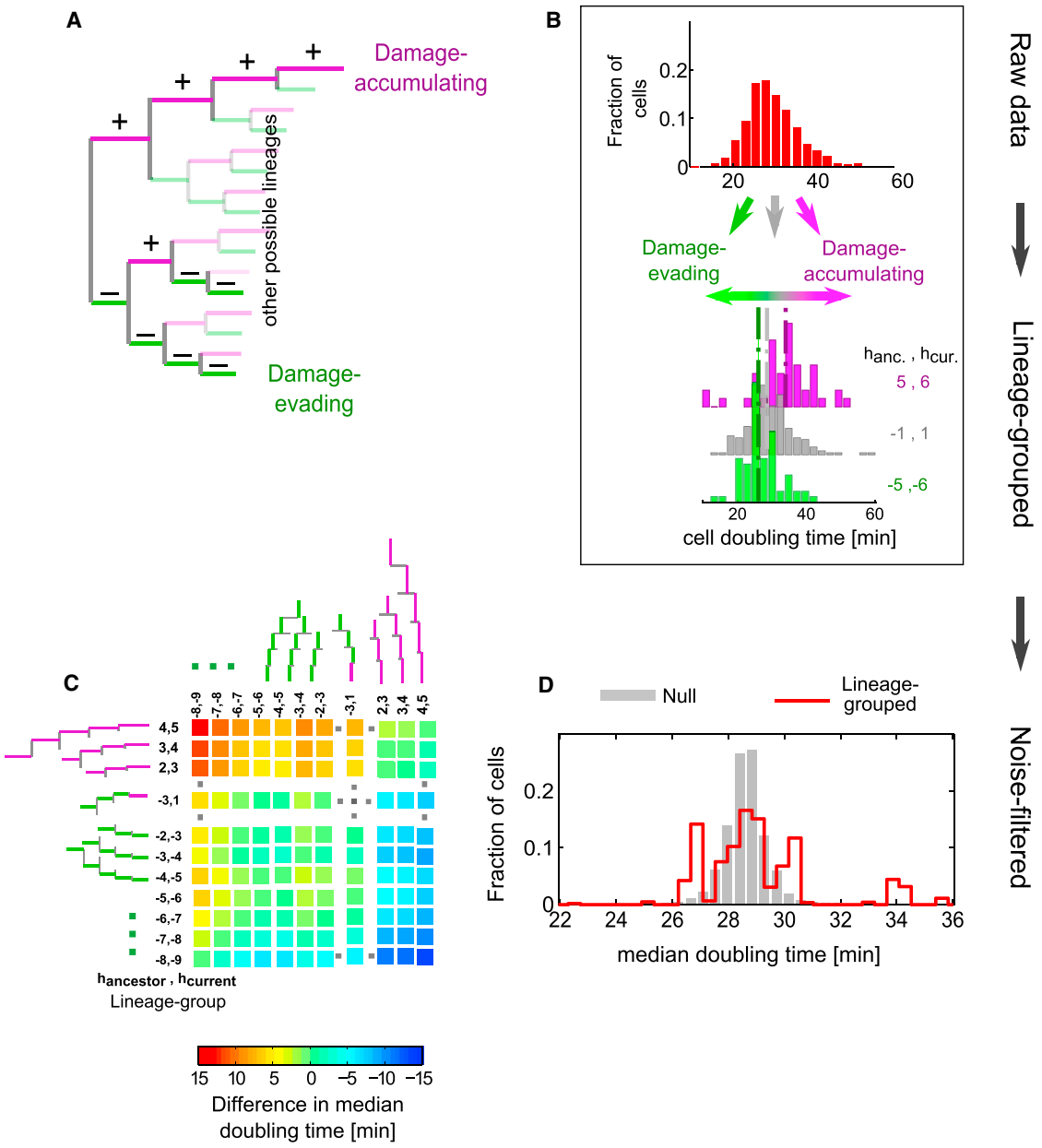

Figure 2. Lineage-Based Approach to Quantify Population Effect of ADS

(A) Each lineage represents a unique history of damage-accumulation (+)/evasion (−) events and therefore results in different doubling times within the population. The extreme, damage-accumulating (all magenta) and damage-evading (all green) lineages are shown.

(B) *Lineage groups* are created by pooling together lineages with similar histories of damage redistribution events. The median doubling times of the each lineage group (dash-dotted lines) are used as a proxy of the noise-filtered doubling time.

(C) The heatmap gives pairwise differences in median doubling times for each pair of lineage groups. We approximate the history of the lineage by a pair of numbers "$h_{ancestor}$, $h_{current}$" where $h_{ancestor}$ is the number of consecutive damage-evasion (−)/accumulation (+) events for the ancestor and $h_{current}$ is the same quantity calculated for the current cell. The entries are symmetric around the diagonal, with a difference only in sign.

(D) Distributions of noise-filtered doubling times. Each value underlying the distribution represents the median doubling time of a lineage group and carries a weight corresponding to the fraction of the population in this group. Null distributions reflect ADS-unrelated variations due to finite sample size and are obtained separately at each stress level by random reshuffling of single-cell doubling times between the lineage groups.

See also Figure S2.

accumulated damage, and we confirmed that the statistical properties of the noise were similar across all lineages. Including all lineages of the population in our analysis (Figure 2B), we obtained a noise-filtered population distribution of doubling times (Figure 2D).

To test this approach, we re-analyzed the low-stress data sampled from a different strain (MG1655) by Stewart et al. (2005). The lineage-based analysis applied to this vast dataset, which consists of over 90 colonies, captures significant differences in doubling times

between lineages differing by only one damage-accumulation/evasion event (Figure S2).

Heat Shock Experiments Confirm Predicted Stress-Adaptive Population Response from ADS

We compared the growth of MC4100Δ*clpB E. coli* expressing ClpB-YFP under minimal stress at 37°C to the heat stress at 42°C. Our data-analysis methods revealed that the doubling time of a cell is indeed highly dependent on its lineage history. We quantified this by the difference in median doubling times between pairs of lineages in Figures 2C, 3A, 3B, and S2. As expected from our model, pairs of lineages with more consecutive damage-accumulating/evading events were characterized by larger time differences. Also, while doubling times did converge to a finite value after successive rounds of damage accumulation (or damage evasion) (Figure S3B), most lineages yielded doubling times that were between the two extremes (Figures 3C and 3D). These observations are in agreement with the model (Figure 1D) and provide experimental confirmation that ADS diversifies cells into numerous subpopulations, and not two subpopulations as suggested earlier (Wang et al., 2010).

Next, we investigated the effects of stress on the distribution of doubling times. We found that the mean doubling time from the noise-filtered data increased for cells exposed to heat stress (from 26.9 at 37°C min to 28.8 min at 42°C, $p < 0.01$ (bootstrapping, see Experimental Procedures), Figures 3C and 3D), which is in agreement with the model (Figure 1B and Equation 2). Moreover, we found that the population diversity (quantified by the width σ of the doubling-time distributions in Figures 3C and 3D and heatmaps in Figures 3A and 3B) is nonzero at low stress (statistically significant compared to the null distribution, see Experimental Procedures) and furthermore increased under the heat stress (from $\sigma_{37} = 1.1$ min to $\sigma_{42} = 2.0$, $p < 0.01$, bootstrapping; see Experimental Procedures and Figure S3A). These findings confirm the stress adaptation predicted by the model.

Taken together, these observations confirm the key model predictions about the population-level effects of ADS. Our results also illustrate that, while ADS is not absent under low levels of stress, it becomes more pronounced at higher stresses. These findings appear to be general, as we have found qualitatively similar results in repeat experiments with antibiotic stress in MC4100Δ*clpB* + ClpB-YFP *E. coli* (0.5 μg/ml kanamycin) (Figures S3C–S3F) and in the parental MC4100 strain under both types of stress (Figures S3G–S3P).

While the stress-induced increase in ADS appears to be general across strains and stress types, the assumed increase in mean doubling time $\langle T \rangle$ is not. This metric actually decreases in WT *E. coli* under 42°C heat shock (Figures S3I–S3K), due to increased ribosomal activity at higher temperatures (Farewell and Neidhardt, 1998). In terms of our model, this means that the minimum doubling time t_{min}, which we assumed to be constant, is in fact environment dependent. We emphasize that variations in t_{min} between different stress levels does not qualitatively affect our findings.

Mechanistic Explanation of Stress-Adaptive Effect of ADS from Aggregate Dynamics

Having confirmed the existence of the stress adaption (manifested by increase in σ), we next investigated the mechanism by which population diversity increases with stress. Our theoretical investigations predicted two different mechanisms (see Equation 3). The first is an increase in the total inheritable damage from each cell $D^{ancestor}$, which is tied to the distribution of damage within the population and thus a signature of population-level response. Second, ADS can also be increased by changes in single-cell response, if the asymmetry parameter, *a,* changes with stress. By distinguishing between the two, one can gain significant insight into mechanisms behind observed ADS.

Consistent with the first mechanism, we found that higher stress was associated with larger amounts of damage, as indicated by the increased frequency and size of fluorescently labeled protein aggregates (see Figures 4B, 4E, S4A, and S4B). However, it was not clear whether this was due to increased aggregate inheritance or solely due to an increased rate of new aggregate formation. Upon closer investigation, we observed that the aggregates became more stable under stress, with half-lives larger than cell doubling times (Figures 4C and S4C). This illustrates that damage inheritance—the fundamental mechanism of ADS—does increase with stress. Moreover, the rate of formation of new aggregates also increased (Figure 4D), and formation occurred equally at each cell pole (Figure S4D), as reported earlier (Lindner et al., 2008). Notably, the frequency of new aggregate formation decreased (Figure S4E), while the probability of finding an aggregate at the old pole increased (Figure S4F) with cell pole age. This could be caused by fusion of misfolded proteins to pre-existing aggregates, similar in effect to aggregate fusion recently reported for *S. pombe* (Coelho et al., 2014) and *M. tuberculosis* (Vaubourgeix et al., 2015). Thus, the data in Figure 4 provide the following mechanistic explanation for stress-adaptive benefit from ADS: higher environmental stress increases the stability and size of aggregates, leading to *larger* differences ΔT between sister cells at division (causing larger σ) and consequently a *stronger* positive feedback amplifying the subpopulation of low-damage cells. As a result, ADS reduces the population doubling time more at higher stress. The increased aggregate formation rate further amplifies the population effect of ADS as more cells experience asymmetric division.

Single-Cell Damage-Dependent Asymmetry at Division Contributes to the Feedback Loop at the Single-Cell Level

We have shown that stress-adaptive effects of ADS can be explained by an increase in heritable damage within the population. However, it was unclear whether this mechanism is sufficient to account for the observed effects. We therefore tested whether the strength of ADS at each stress level could be explained solely by the stress parameter, λ, assuming no change in the asymmetry parameter, a. We used the difference in doubling times $\Delta\overline{T}$ of the extreme lineages to fit our model (the damage-accumulating and damage-evading lineages highlighted by thick magenta and green lines in Figure 1A, Supplemental Experimental Procedures, III.6). The model successfully captured most of the features in $\Delta\overline{T}$ (dashed lines in Figure 5A) and passed two validation criteria. First, it reproduced the increased difference in doubling times at higher stress. Second, it captured the near-linear

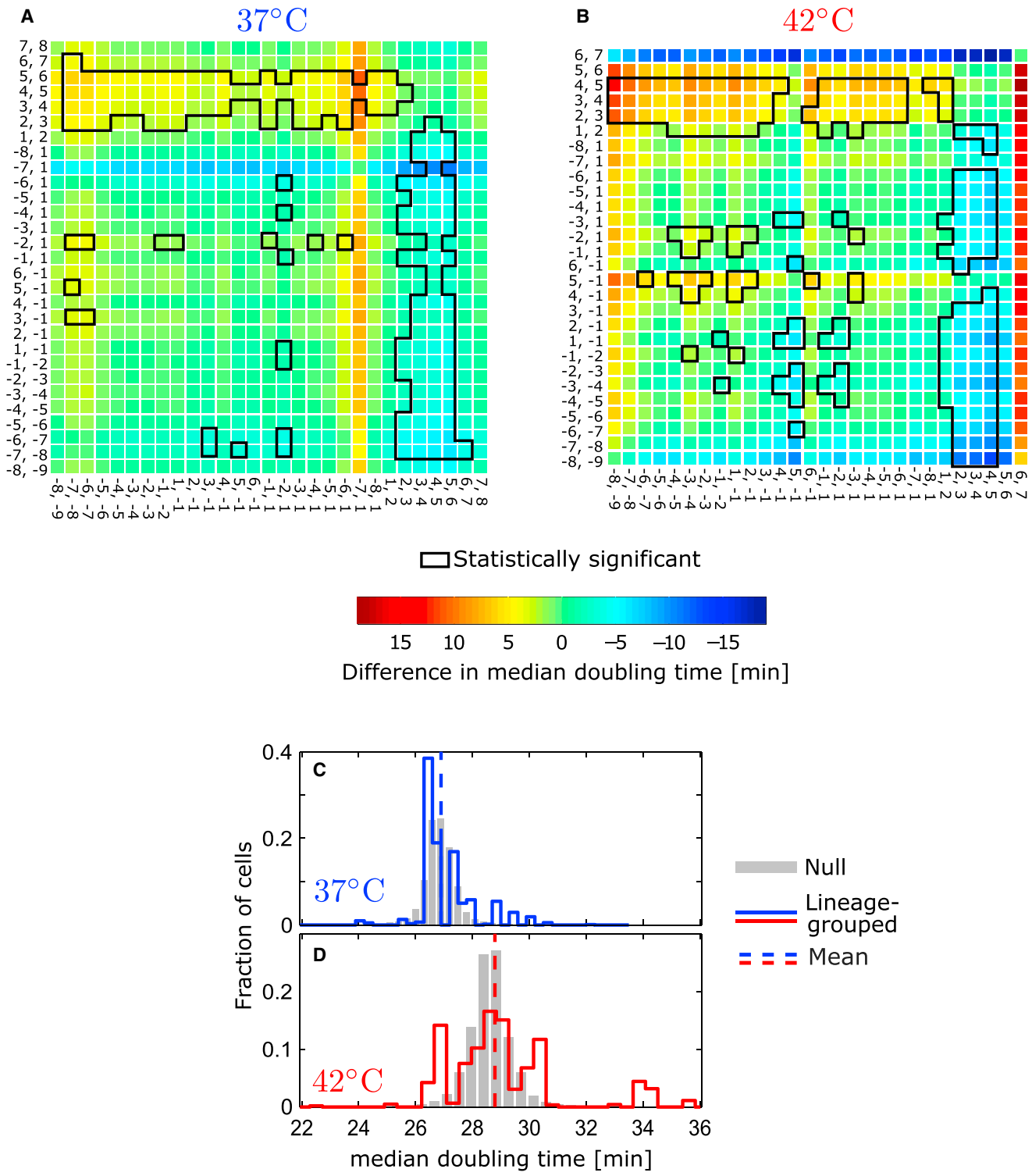

Figure 3. ADS Signatures at Low and High Stress

(A and B) Heatmaps of pairwise differences in median doubling times at 37°C and 42°C show that differences between lineage groups are larger under heat stress. Statistically significant entries are outlined in black.

(C and D) Noise-filtered distributions of doubling times at 37°C and 42°C. The mean and the width of the distribution are larger under heat stress.

See also Figure S3.

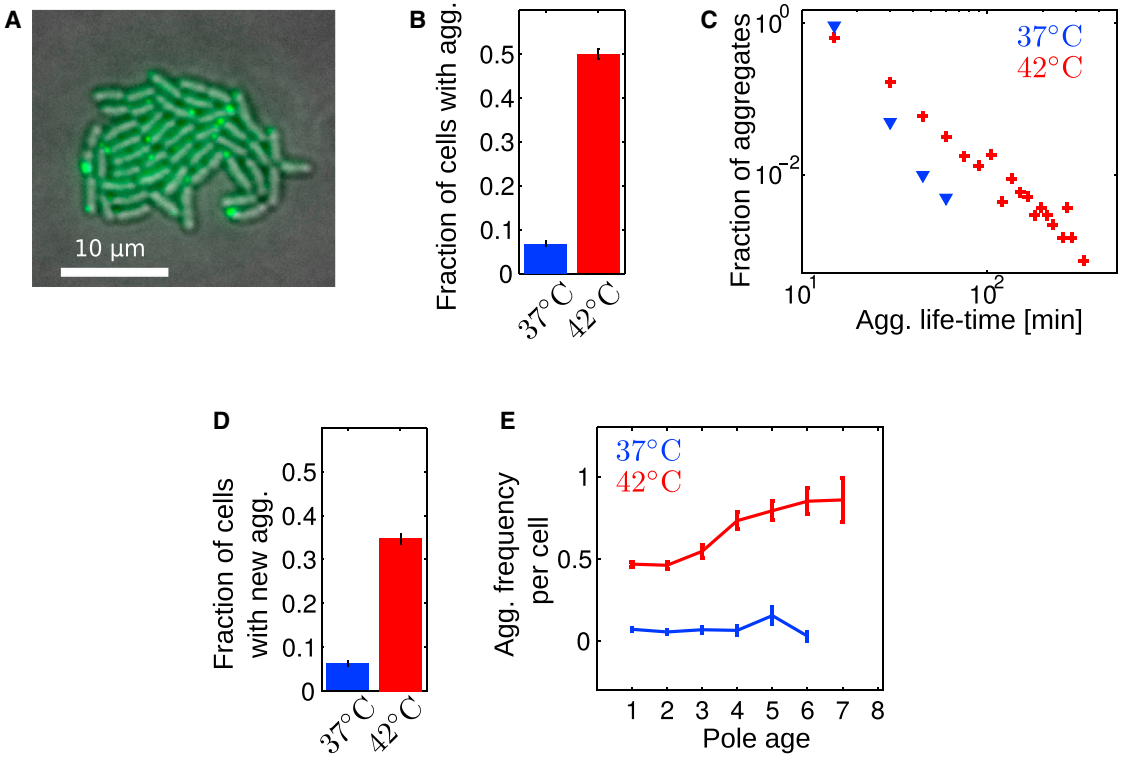

Figure 4. Aggregate Dynamics Provides the Mechanism of Stress-Adaptive ADS

(A) Representative bright-field image of *E. coli* cells (MC4100ΔclpB) with fluorescence image of ClpB-YFP overlaid in green; fluorescent foci mark protein aggregates (Winkler et al., 2010).

(B) Fraction of cells with protein aggregates. More cells harbor aggregates at higher stress. Here and in (D) and (E), error bars indicate the SE of the frequency caused by the finite counting statistics (see Experimental Procedures).

(C) Distribution of aggregate lifetimes. Aggregates are longer lived at higher stress, with very few aggregates persisting longer than a mean doubling time of ~27 min under low stress.

(D) Fraction of cells with newly formed aggregates. Aggregates form at a higher rate under stress.

(E) Frequency of aggregates per cell as a function of pole age (mean with error bars showing 95% confidence interval) is constant around 0.1 and independent of pole age for low stress (blue) but exhibits a strong dependence on pole age and a much higher level at higher stress (red). Only pole ages where at least one aggregate was detected have been included.

See also Figure S4.

relationship between $\Delta\overline{T}$ at low and high stress we observed in experimental data (Figure S5A and Supplemental Information, section IV.6.2). However, it failed to fit the data for the early pole ages (Figure 5A). Furthermore, the fit did not improve when the asymmetry parameter, *a,* was fitted independently at each stress level.

The relatively poor fit of the model with constant asymmetry *a* suggested that the increase in stress alone is insufficient to explain the increase in observed ADS. We therefore considered the possibility that *a* could have a more complex dependency on stress or damage levels. To test this, we analyzed the inheritance of aggregates as a function of pole age. If *a* is constant, then the probability of aggregate inheritance should not depend on the pole age. However, Figure 5B shows that older-pole cells have a higher probability of retaining aggregates following division. Contrary to the underlying assumption of most previous studies (Erjavec et al., 2008; Wang et al., 2010; Ackermann et al., 2007; Watve et al., 2006; Rang et al., 2012), *a* is not the same for all cells in a population, but depends on the pole age and the amount of accumulated damage in the cell. Aggregate inheritance at the single-cell level is mostly binary because cells typically have either zero or one aggregate (the frequency is less than 1 in Figures 4E and S4B). However, the averaged damage-dependent asymmetry measured from aggregate inheritance follows a sigmoidal, Hill-like function (Figures 5C, S5B, and S5C), described by Equation 4 (constant c_3 corresponds to hill coefficient, c_1 and c_2 control the offset and the inflection point, best-fit values are given in Figure S5C).

$$a(D) = \frac{c_1 + D^{c_3}}{c_2 + D^{c_3}}. \qquad \text{(Equation 4)}$$

The damage-dependent asymmetry is a direct consequence of long-lived aggregates passively migrating to the old pole after a few divisions, as described by Lindner et al. (Lindner et al., 2008) (see also Figure S4F). This occurs because aggregates, which initially form anywhere in the cell, will get pushed toward the cell poles due to nucleoid occlusion (Winkler et al., 2010; Potten et al., 2002). Furthermore,

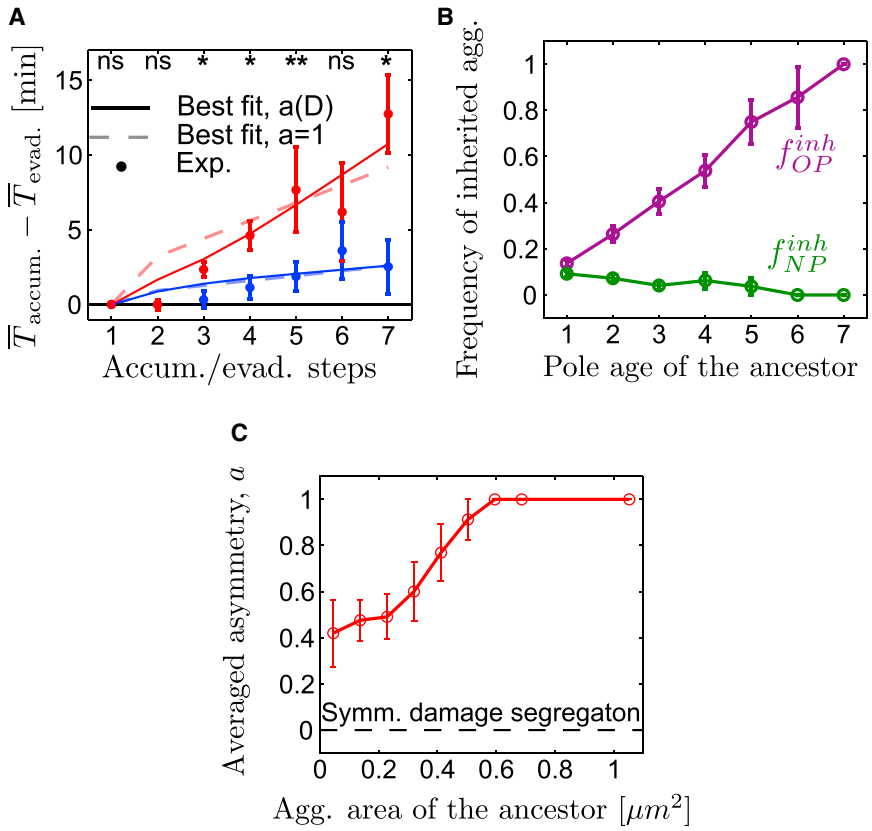

Figure 5. Experimental Evidence for Damage-Dependent Asymmetry

(A) The difference in experimental doubling times between the damage-accumulating and damage-evading lineages starting from the same cell. Error bars indicate the SEM. The dashed lines show the fit of the "constant *a*" model, while the solid lines show the fit of the "*a*(*D*) model" (see Experimental Procedures).

(B) Frequencies of inherited aggregates f_{NP}^{inh} and f_{OP}^{inh} of new-pole and old-pole lineages at 42C illustrate an increasing probability of aggregate inheritance with pole age of old-pole lineages and near-constant frequency for new-pole lineages. We do not plot the values for low stress, since the aggregates did not typically persist for multiple generations. Error bars indicate SE of the frequency (see Experimental Procedures).

(C) Asymmetry measured by area of aggregates at division plotted as a function of the aggregate area of ancestor.

See also Table S2 and Figure S5. Error bars indicate SE.

the non-linearity of the stress dependent asymmetry may result from a combined effect of larger aggregates diffusing slower (Potten et al., 2002), as well as recently reported fluid-to-glass like transition of the bacterial cytoplasm (Parry et al., 2014) contributing to further immobilization of the larger aggregates. Thus, damage-dependent asymmetry is a single-cell emergent property arising – without any cellular regulation – when an aggregate is inherited sufficiently many times.

To confirm that single-cell damage-dependent asymmetry indeed improves the model, we included this feature (Equation 4 with parameters as in Figure S5C) and refitted to the experimental data of $\Delta\overline{T}$ (Figure 5A, full lines). We found that these fits were statistically significantly better under high stress compared to the previous attempt (dashed lines). The goodness of the fit and the statistical significance was quantified according to the Akaike model selection criteria – a statistical aid when choosing between the competing models (Burnham and Anderson, 2002) (Supplemental Information, section III.9; Table S2). The discrepancy between the adaptive asymmetry *a(D)* model and the experimental data at one to two consecutive accumulation/evasion events likely arise because *a* cannot be measured for small aggregates below the detection limit. In the simulations, we have set *a(D)* to follow Equation 4. for all aggregate sizes. However, the actual asymmetries may be lower for small aggregates, e.g., due to their shorter half-life and faster diffusion. Also, at low aggregate numbers, stochastic effects not included in our model might cause discrepancies.

The adaptive asymmetry *a*(*D*) model also provided a better fit for both the MC4100ΔclpB + ClpB-YFP and WT strain under both stress types (Figure S5D; Table S2). Both the mechanistic insights in Figure 4 and the evidence that aggregates tend to merge (reported in *E. coli* (Lindner et al., 2008) and fission yeast (Coelho et al., 2014)) suggest that the damage-dependent asymmetry may not be limited to *E. coli*.

Population-Level Benefits from ADS Persist under Noise

The significant ADS-unrelated cell-to-cell variations in doubling times ($\sigma_{noise}^{42C} = 6.8$ min, see Figure S5E) compared to the effect of ADS ($\sigma_{ADS}^{42C} = 2.1$ min) casts doubt on the relevance of ADS. We explore the effect of this noise, and found that the benefit of ADS is still significant. First, while the overall effect of ADS on population diversity, σ, is comparable to the noise, ADS consistently showed a larger response to stress (1.8-fold compared to 1.3-fold for coefficient-of-variance, see Supplemental Information, section III.10; Figures S3A, S3F, S3L, and S3P). Second, simulations incorporating physiological levels of noise into our experimentally validated model indicated that the benefits of ADS, in terms of mean doubling time and population damage, are significant even in the presence of this large noise (see Figure 6A). The benefits of ADS also increased with stress level in our simulations, just as our noise-free theory predicted (Figure 1C).

The effects of ADS on doubling times were masked by noise at small population sizes in the simulations (Figure 6A, $n \sim 9$). However, differences in damage inheritance were amplified along the lineages and were detectable after a few generations (Figure 6A, $n \sim 5{,}000$). Therefore, the population-level benefits of ADS emerge for biologically reasonable population sizes, even when ADS-unrelated growth variance (Figure S5E) dominates at the level of sister pairs.

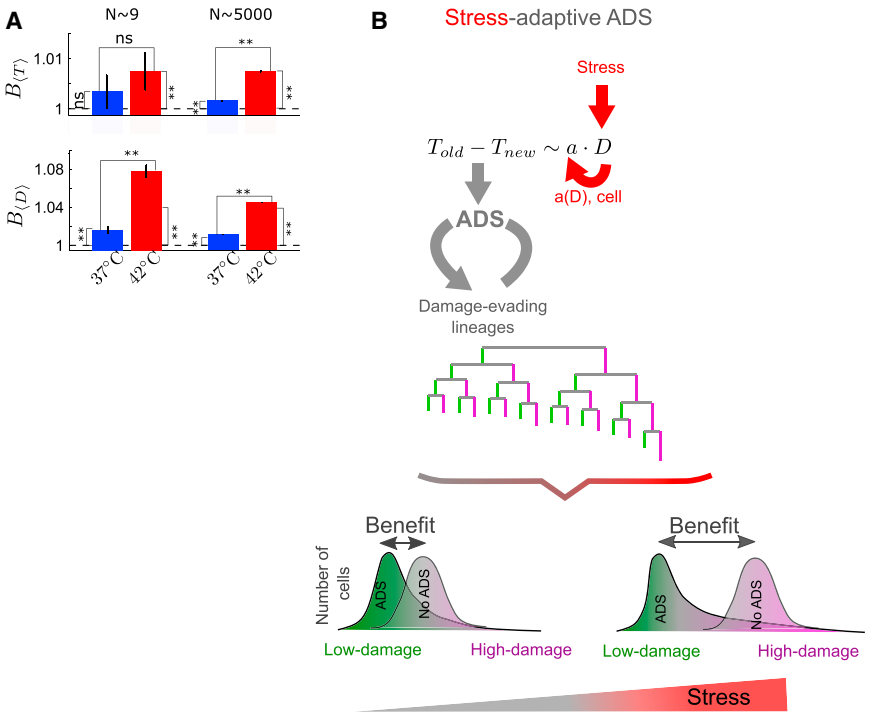

Figure 6. Population and Single-Cell Feedbacks Ensure Population Benefit from ADS

(A) Estimates of the population benefits from ADS when accounting for ADS-unrelated cell-to-cell variations (model simulations with parameters derived from experimental data). The population benefits are significantly different for large population of $n \approx 5,000$ cells but not for small populations of $n \approx 9$ cells. The error bars indicate the SE across 10^3 repeat simulations. Top: doubling-time benefit, $B_{\langle T \rangle}$, taken as fold decrease in mean doubling time in presence of ADS as compared to no ADS. Bottom: damage benefit, $B_{\langle D \rangle}$, taken as fold decrease in mean damage levels (see Experimental Procedures for exact expressions). **Significant difference of the mean (t test, $p < 0.01$), *(t test, $p < 0.05$), ns, not significant (t test, $p > 0.05$).

(B) Summary of the single-cell and population-level stress-adaptive ADS. Stress increases the difference between sister cells, $T_{old} - T_{new}$, either directly on whole-population level by increasing the amount of accumulated damage, $D^{ancestor}$, or indirectly, on a single-cell level, by damage-dependent asymmetry at division, $a(D)$. On a population level, the difference in doubling times across lineages creates an ADS-mediated positive feedback. Resulting is a stress-adaptive strategy amplifying the proportion of low-damage cells, while concentrating most of the damage in a few cells.

DISCUSSION

Macromolecular damages are unavoidable by-products of cellular functioning and are known to be associated with aging and various human disorders (Tyedmers et al., 2010). While single-cell ADS has been known for the last decade, its role (if any) in mitigating the effects of stress has remained obscure. Here, we combined theoretical and in silico modeling with experiments and analysis methods to uncover a population stress response emerging due to ADS – an adaptive population stress response. This adaptive population stress response, which arises in a completely self-organized fashion when the population is exposed to environmental stress, may be summarized as follows (Figure 6B). At each division, a difference in doubling times between the two resulting cells is set up by ADS (Equation 3). This difference is amplified within the population as progeny from the faster-growing sister inherit less damage and therefore divide more often, resulting in an over-representation of low-damage cells. As a result, there is a positive feedback that acts on low-damage cells within a population. The stress-adaptation arises from acceleration of the positive feedback under high stress, due to an increase in inheritable damage $D^{ancestor}$. The inheritable damage is the damage that escaped the repair. The increased amounts of $D^{ancestor}$, due to increased rate of accumulation and stability (Figure 4; Clegg et al., 2014), reflect the limitations of the repair mechanisms.

Adaptation is further improved via damage-dependency of the asymmetry parameter a. The extent to which this asymmetry is due to binary effects (e.g., frequency of aggregate inheritance) or graded effects (e.g., size of inherited aggregates) is still unclear. Nevertheless, the similarity of aggregate dynamics under both heat and antibiotic stresses (Figures S4A–S4C) suggest that aggregate formation and inheritance is functionally similar across different stresses. These results in combination with research on *S. pombe* (Coelho et al., 2014), indicate that damage-dependent asymmetry is likely a general feature of ADS and is not specific to a specific type of cell.

Dynamic Picture of Damage-Distribution Questions Previous Analyses of ADS

Our results provide a new dynamic picture of how damage is distributed within a population, with redistribution at each cell division that imparts structure to the population as a whole. This picture stands in contrast with earlier studies. Wang et al. (Wang et al., 2010) suggested that the entire population converges toward the fixed doubling time because the doubling time of aging cells converges toward such a finite value. The work by Rang et al. (Rang et al., 2011) reinterpreted their data and proposed that cells converge to two steady states, one with a doubling time of a fully rejuvenated cell, often likened to a gamete cell, and the other of the most "aged" cell within the population (the somatic cell). A consequence of this simplification is that every division can be thought of as producing one of each of these cell types, and the intermediate cell types could be ignored. While the somatic cell- germ cell paradigm is a useful conceptual tool, we found that seemingly binary events such as single-aggregate inheritance (Figure 4E) do not result in two distinct subpopulations of cells. Since the size of the aggregates increases within each generation (Figure S4A) the changes in damage and division times across lineages are graded, not binary. So while a few extreme branches (consecutively accumulating/evading lineages; referred to as new- and old-pole attractors by Rang et al., 2011) eventually converge to fixed

damage levels (indicated by doubling times in Figure S3B and reported in Wang et al., 2010), most of the lineages are constantly moving in between these two extremes according to their sequence of damage-accumulation and damage-evasion events (e.g., Figures 3C and 3D). Nonetheless, the population is in a dynamic equilibrium where the overall damage distribution remains constant in time.

Another reason for examining population structure when quantifying ADS is that metrics such as cell doubling time are environment and strain dependent. This observation has an important consequence for the choice of a right ADS measure: while the change in t_{min} between strains and environments does not affect distribution widths σ as it is based on difference in doubling times (see Equation 3), it does perturb the ratio of sister doubling times – a commonly used metric of ADS. (For illustration, consider the case of full asymmetry, $a = 1$ when newly acquired damage has a small contribution to the doubling time, $\mu\lambda \ll t_{min}$. The ratio of sister doubling times $T_{old}/T_{new} = (t_{min} + \mu D^{ancestor})/t_{min}$ is strongly affected by t_{min}).

Population-Level Effects of ADS May Apply More Generally: Predictions and Implications for Observed Asymmetric DNA and Aggregate Segregation in Stem Cells

While this work has focused on ADS in *E. coli*, our framework and predictions are likely to apply more generally to any self-amplifying heritable traits, including any cell population subject to macromolecular damage. A particularly intriguing candidate is the Immortal Strand Hypothesis (ISH) for adult stem cell populations (or alternatively, the Silent Sister Hypothesis). ISH predicts that stem cells will minimize the accumulation of errors within their DNA through retention of template DNA following division. The replicated DNA, which will incur replicative errors, is passed on to a less multipotent, or terminally differentiated, daughter cell. As a result, the total number of mutations within all cells is minimized. Our mathematical framework can be used to track the accumulation of mutations through each lineage. λ would correspond to the frequency of mutations due to replicative errors, and t_{min} would correspond to spontaneous mutation of non-replicating DNA. In this case, it is not the doubling time of each cell, but the length of each lineage that would be damage- dependent. High-damage lineages would consist of fewer cell-doubling events, as per ISH these cells are more likely to differentiate and exit the stem-cell pool. We would expect that the ISH in this model will result in a reduced mutational load in a population of adult stem cells.

Although the analogy between the protein aggregates and mutational frequency has a number of limitations and there are many experimental difficulties in using a lineage-based approach to test the ISH, such as incomplete knowledge of differentiation hierarchies or lack of effective DNA probes, we urge caution in drawing conclusions from cell-pairs alone. We expect that, as in the case of ADS in *E. coli*, strand retention does not create two distinct populations of cells – the mutation-free DNA of stem cells, and the mutated DNA of differentiated cells. Strand retention will impose a much more graded change in mutational frequency across all cells, requiring a population-level analysis.

When applied to DNA and aggregate segregation in stem cells, the lineage-based analysis may resolve ADS effects that are currently below detection limit and thus reveal why ADS manifestation is environment and cell type-specific (Bufalino et al., 2013; Rujano et al., 2006; Yennek et al., 2014; Conboy et al., 2007).

EXPERIMENTAL PROCEDURES

Cell Lines and Fluorescent Reporter

We performed experiments with the *E. coli* strain MC4100 (Smith, 2005) and a deletion mutant for clpB, which encodes a protein involved in disassembly of aggregates of misfolded proteins (Winkler et al., 2010). To visualize protein aggregates, mutant cells were transformed with a plasmid containing YFP-tagged ClpB (pHSG ClpB-YFP) under the lac promoter together with a plasmid containing constitutively expressed lacI (pBB529).The reporter was induced by supplying IPTG (200 μM). Our "wild-type" cells were MC4100 transformed with the pBB529 plasmid for selection purposes grown without the inducer. Plasmids and the MC4100ΔclpbB strain were kindly donated by Juliane Winkler. See Supplemental Experimental Procedures for details.

Experiments, Microscopy, and Image Analysis

Freshly inoculated cells were grown overnight in a heat-controlled shaking incubator under the prescribed stress level. For the experiments, exponential-phase cells were plated on freshly made agarose (1.5%, including inducers and antibiotic stressors when appropriate), which was placed directly on a microscope coverslip and sealed from the external environment using a custom setup, enabling stable experimental conditions over extended periods of time. We imaged the cells using 100× objective every 3–4 min in bright field and every ~15 min in fluorescence (only mutant cells) on a temperature-controlled microscope. The images were analyzed using custom image analysis software. Image analysis provided single-cell growth rates and aggregate dynamics together with pedigree. Single-cell growth rates γ were obtained from experimental measurements of single-cell length as a function of time $\ell(t)$ by fitting to exponential function $\ell(t) = \ell_0 e^{\gamma t}$. Filters were applied to ignore cells with too few or corrupted data points. Single-cell doubling times T were computed from accepted growth rates as

$$T = \frac{\ln 2}{\gamma}.$$

Aggregates were accepted if their average fluorescence intensity was at least 1.6 times the average cell intensity. Each experiment yielded eight to 14 independent colonies and was repeated at least once on a separate day using freshly inoculated cells. See Supplemental Experimental Procedures and Table S1, summarizing all reported experiments, for details.

Statistical Analyses

The width of the distribution of doubling times is $\sigma = \sqrt{\langle (T - \langle T \rangle)^2 \rangle}$. For normally distributed data, this definition is equivalent to the SD. However, we specifically refrain from using this terminology since most of our distributions are skewed and highly non-normal.

Averages

Population averages of some quantity X are denoted by angle brackets $\langle X \rangle$, and averages over all cells in a lineage group (defined above) are denoted by an overline, $\overline{X}$. The lineage-group averages are used to filter away non-ADS-related noise in the experimental data. In Figure 5A, multiple lineage pairs were analyzed per micro-colony.

The Error Introduced by Lineage Grouping

The histories of lineages pooled together in the same lineage group are similar, but not identical. This results in a small variation in doubling times among lineages within the same group even in the absence of noise. By running computer simulations at different values of asymmetry and stress, we find this variation, quantified by coefficient of variation (CV), is below 2% (with only two bins above 1%) and is considerably smaller than the variations introduced by noise (CV ~20%) or typical significant changes between bins across our experiments (15%–50%).

Aggregate Statistics

Very few cells were observed to have more than one aggregate, and under low-stress conditions many cells had none. Thus, we analyzed aggregate presence/absence at the single-cell level under the approximating assumption

that it follows a binomial distribution using the corresponding standard formulae: at any pole age, j, for the case of N^j_{agg} aggregates and N^j_{cells} cells, the fraction of cells with aggregates is $f_j = (N^j_{agg}/N^j_{cells})$ and the SE of the frequency $\sigma_{f_j} = \sqrt{(f_j(1-f_j)/N^j_{cells})}$.

Significant Differences of Mean Doubling Times from Different Stresses

We used bootstrapping to obtain statistical significance when comparing the difference of mean doubling times at two conditions (Figures 3C and 3D, dashed lines) since the underlying distributions were noticeably non-normal. We separately resampled the data with replacement at each of the two conditions, thereby obtaining a single estimate of the mean value from each distribution. We repeated this process 10^4 times, each time obtaining a mean value from each distribution. For each of the 10^4 repeats, we then subtracted the mean value from one condition from its sister at the other condition, resulting in a normal distribution of differences between the mean of the two original distributions, which we compared against the null hypothesis of zero mean using a t test.

Null Distributions and Significant Differences of Distribution Width σ

Null distributions for population growth rates (Figures 3C and 3D, gray bars) were obtained by reshuffling doubling times between lineage groups, taking the mean, and repeating a total of 500 times. Increases in population width with stress were also obtained via bootstrapping by randomly sampling the underlying distributions at low and high stress and comparing to the same result from the null distribution, repeating the process a total of 10^4 times.

Single-Cell Statistics

Distributions of single-cell doubling times were not normal, so we used bootstrapping to obtain SEM: we resampled the data with replacement to obtain a single estimate of the population mean, and repeat a total of 10^4 times. The resulting distribution of means follows a normal distribution and is thus well characterized by its SD.

All statistical analyses were and simulations were performed in MATLAB (2012b), with details of the statistical procedures given in Supplemental Experimental Procedures.

Theoretical Results

Theoretical Results are given in Supplemental Experimental Procedures, section VI. In Figure 1B, we used Equation S7 for $\langle T \rangle$ and Equation S8 for σ in Figure 1E. In Figure 5A, we used Equation S3 to describe $\Delta\overline{T}$. Details of theoretical derivations will be published elsewhere.

Numerical Simulations of the Model

The models have been implemented as agent-based simulations. In all reported cases, we have started the simulations from a single cell with no inherited damage. To simulate the growing population, we first construct the entire population tree for a specified number of generations. Next, for each cell in the tree, we compute and record the cell's damage and doubling time as given in Equation 1 and 2 and add small zero-mean noise to the doubling times for faster convergence. For further details, see Supplemental Experimental Procedures, section IV.

Population Benefit from ADS, $B_{\langle T \rangle}$, and $B_{\langle D \rangle}$

The benefit in reducing the population mean doubling time due to ADS, $B_{\langle T \rangle} = (\langle T \rangle_{a=0}/\langle T \rangle_{a\geq 0})$ is defined as the fold-change decrease in mean doubling time $\langle T \rangle_{a\geq 0}$ in a population dividing damage with some asymmetry $(a \geq 0)$, relative to mean doubling time $\langle T \rangle_{a=0}$ in a population dividing damage symmetrically $(a = 0)$. Similarly, the benefit in reducing the population mean damage levels: $B_{\langle D \rangle} = (\langle D \rangle_{a=0}/\langle D \rangle_{a\geq 0})$.

Fitting Experimental Data Using Model and Simulations

To fit our model to the data in Figure 5A, we let the two stress levels λ_L (low stress) and λ_H (high stress) be free parameters but required that μ be the same for both low and high stress. The ADS-free minimum generation time t_{min} is also a free parameter, but its value has no implication on $\Delta\overline{T}$ and so it cannot be determined. We set it to the plausible value $t_{min} = 22$ in our model (obtain same results by varying it within reasonable bounds). Fitting was performed using the least-squares fitting routine lsqcurvefit in MATLAB. For the case of damage-dependent asymmetry, we simulated the model numerically with $a(D)$ taken from Equation 3 (parameters in Figure S5C) during the fitting routine, requiring μ to be the same at low and high stress.

SUPPLEMENTAL INFORMATION

Supplemental Information includes Supplemental Experimental Procedures, five figures, and two tables and can be found with this article online at http://dx.doi.org/10.1016/j.cels.2016.06.008.

AUTHOR CONTRIBUTIONS

A.T., S.V., and H.N. conceived and performed experiments, analyzed the data, and wrote manuscript. A.K. contributed to mathematical model and wrote the manuscript. S.S. contributed to the experiments and wrote the manuscript. A.T. secured funding.

ACKNOWLEDGMENTS

We thank Juliane Winkler for sharing plasmids and MC4100 strain and Eric J. Stewart for sharing data. We furthermore thank Kim Sneppen, Namiko Mitarai, Kenn Gerdes, and Anne Grapin-Botton for their input. A.T., S.S., and H.N. were funded by the Danish National Research Foundation (C-MOL and StemPhys Centers). S.V. was funded by Niels Bohr International Academy Postdoctoral Fellowship.

Received: July 31, 2015
Revised: April 5, 2016
Accepted: June 16, 2016
Published: July 14, 2016

REFERENCES

Ackermann, M., Chao, L., Bergstrom, C.T., and Doebeli, M. (2007). On the evolutionary origin of aging. Aging Cell *6*, 235–244.

Aguilaniu, H., Gustafsson, L., Rigoulet, M., and Nyström, T. (2003). Asymmetric inheritance of oxidatively damaged proteins during cytokinesis. Science *299*, 1751–1753.

Bufalino, M.R., DeVeale, B., and van der Kooy, D. (2013). The asymmetric segregation of damaged proteins is stem cell-type dependent. J. Cell Biol. *201*, 523–530.

Burnham, K.P., and Anderson, D.R. (2002). Model Selection and Multimodel Inference: A Practical Information-Theoretic Approach (Springer).

Chao, L. (2010). A model for damage load and its implications for the evolution of bacterial aging. PLoS Genet. *6*, e1001076.

Clegg, R.J., Dyson, R.J., and Kreft, J.U. (2014). Repair rather than segregation of damage is the optimal unicellular aging strategy. BMC Biol. *12*, 52.

Coelho, M., Dereli, A., Haese, A., Kühn, S., Malinovska, L., DeSantis, M.E., Shorter, J., Alberti, S., Gross, T., and Tolić-Nørrelykke, I.M. (2013). Fission yeast does not age under favorable conditions, but does so after stress. Curr. Biol. *23*, 1844–1852.

Coelho, M., Lade, S.J., Alberti, S., Gross, T., and Tolić, I.M. (2014). Fusion of protein aggregates facilitates asymmetric damage segregation. PLoS Biol. *12*, e1001886.

Conboy, M.J., Karasov, A.O., and Rando, T.A. (2007). High incidence of non-random template strand segregation and asymmetric fate determination in dividing stem cells and their progeny. PLoS Biol. *5*, e102.

Erjavec, N., Cvijovic, M., Klipp, E., and Nyström, T. (2008). Selective benefits of damage partitioning in unicellular systems and its effects on aging. Proc. Natl. Acad. Sci. USA *105*, 18764–18769.

Farewell, A., and Neidhardt, F.C. (1998). Effect of temperature on in vivo protein synthetic capacity in Escherichia coli. J. Bacteriol. *180*, 4704–4710.

Fuentealba, L.C., Eivers, E., Geissert, D., Taelman, V., and De Robertis, E.M. (2008). Asymmetric mitosis: Unequal segregation of proteins destined for degradation. Proc. Natl. Acad. Sci. USA *105*, 7732–7737.

Iyer-Biswas, S., Wright, C.S., Henry, J.T., Lo, K., Burov, S., Lin, Y., Crooks, G.E., Crosson, S., Dinner, A.R., and Scherer, N.F. (2014). Scaling laws governing stochastic growth and division of single bacterial cells. Proc. Natl. Acad. Sci. USA *111*, 15912–15917.

Kaganovich, D., Kopito, R., and Frydman, J. (2008). Misfolded proteins partition between two distinct quality control compartments. Nature *454*, 1088–1095.

Lindner, A.B., Madden, R., Demarez, A., Stewart, E.J., and Taddei, F. (2008). Asymmetric segregation of protein aggregates is associated with cellular aging and rejuvenation. Proc. Natl. Acad. Sci. USA *105*, 3076–3081.

Liu, B., Larsson, L., Franssens, V., Hao, X., Hill, S.M., Andersson, V., Höglund, D., Song, J., Yang, X., Öling, D., et al. (2011). Segregation of protein aggregates involves actin and the polarity machinery. Cell *147*, 959–961.

Malinovska, L., Kroschwald, S., Munder, M.C., Richter, D., and Alberti, S. (2012). Molecular chaperones and stress-inducible protein-sorting factors coordinate the spatiotemporal distribution of protein aggregates. Mol. Biol. Cell *23*, 3041–3056.

Parry, B.R., Surovtsev, I.V., Cabeen, M.T., O'Hern, C.S., Dufresne, E.R., and Jacobs-Wagner, C. (2014). The bacterial cytoplasm has glass-like properties and is fluidized by metabolic activity. Cell *156*, 183–194.

Potten, C.S., Owen, G., and Booth, D. (2002). Intestinal stem cells protect their genome by selective segregation of template DNA strands. J. Cell Sci. *115*, 2381–2388.

Rang, C.U., Peng, A.Y., and Chao, L. (2011). Temporal dynamics of bacterial aging and rejuvenation. Curr. Biol. *21*, 1813–1816.

Rang, C.U., Peng, A.Y., Poon, A.F., and Chao, L. (2012). Ageing in Escherichia coli requires damage by an extrinsic agent. Microbiology *158*, 1553–1559.

Rujano, M.A., Bosveld, F., Salomons, F.A., Dijk, F., van Waarde, M.A., van der Want, J.J., de Vos, R.A., Brunt, E.R., Sibon, O.C., and Kampinga, H.H. (2006). Polarised asymmetric inheritance of accumulated protein damage in higher eukaryotes. PLoS Biol. *4*, e417.

Smith, G.H. (2005). Label-retaining epithelial cells in mouse mammary gland divide asymmetrically and retain their template DNA strands. Development *132*, 681–687.

Specht, S., Miller, S.B., Mogk, A., and Bukau, B. (2011). Hsp42 is required for sequestration of protein aggregates into deposition sites in Saccharomyces cerevisiae. J. Cell Biol. *195*, 617–629.

Spokoini, R., Moldavski, O., Nahmias, Y., England, J.L., Schuldiner, M., and Kaganovich, D. (2012). Confinement to organelle-associated inclusion structures mediates asymmetric inheritance of aggregated protein in budding yeast. Cell Rep. *2*, 738–747.

Stewart, E.J., Madden, R., Paul, G., and Taddei, F. (2005). Aging and death in an organism that reproduces by morphologically symmetric division. PLoS Biol. *3*, e45.

Tyedmers, J., Mogk, A., and Bukau, B. (2010). Cellular strategies for controlling protein aggregation. Nat. Rev. Mol. Cell Biol. *11*, 777–788.

VanBogelen, R.A., and Neidhardt, F.C. (1990). Ribosomes as sensors of heat and cold shock in Escherichia coli. Proc. Natl. Acad. Sci. USA *87*, 5589–5593.

Vaubourgeix, J., Lin, G., Dhar, N., Chenouard, N., Jiang, X., Botella, H., Lupoli, T., Mariani, O., Yang, G., Ouerfelli, O., et al. (2015). Stressed mycobacteria use the chaperone ClpB to sequester irreversibly oxidized proteins asymmetrically within and between cells. Cell Host Microbe *17*, 178–190.

Wang, P., Robert, L., Pelletier, J., Dang, W.L., Taddei, F., Wright, A., and Jun, S. (2010). Robust growth of Escherichia coli. Curr. Biol. *20*, 1099–1103.

Watve, M., Parab, S., Jogdand, P., and Keni, S. (2006). Aging may be a conditional strategic choice and not an inevitable outcome for bacteria. Proc. Natl. Acad. Sci. USA *103*, 14831–14835.

Winkler, J., Seybert, A., König, L., Pruggnaller, S., Haselmann, U., Sourjik, V., Weiss, M., Frangakis, A.S., Mogk, A., and Bukau, B. (2010). Quantitative and spatio-temporal features of protein aggregation in Escherichia coli and consequences on protein quality control and cellular ageing. EMBO J. *29*, 910–923.

Yennek, S., Burute, M., Théry, M., and Tajbakhsh, S. (2014). Cell adhesion geometry regulates non-random DNA segregation and asymmetric cell fates in mouse skeletal muscle stem cells. Cell Rep. *7*, 961–970.

Zhou, C., Slaughter, B.D., Unruh, J.R., Eldakak, A., Rubinstein, B., and Li, R. (2011). Motility and segregation of Hsp104-associated protein aggregates in budding yeast. Cell *147*, 1186–1196.

Cell Systems, Volume *3*

Supplemental Information

Asymmetric Damage Segregation Constitutes an Emergent Population-Level Stress Response

Søren Vedel, Harry Nunns, Andrej Košmrlj, Szabolcs Semsey, and Ala Trusina

I. CELL CULTURE AND TIME-LAPSE MICROSCOPY

Cells were inoculated from the LB agarose plate in M63 minimal media with selection markers and were grown overnight at the specified temperature in 10 mL tubes in a shaking incubator. Cells were diluted into fresh media (with selection markers etc.) in the morning and left for $\sim$ 2.5 h in the incubator to reach the exponential phase. Experiments were commenced following another dilution.

Low-density cells were transferred to a 1.5% agarose pad (containing all relevant selection markers, antibiotics etc. in same concentrations as in the liquid culture), which was inverted and placed directly on a microscope cover slip (No. 1.5) and sealed with an air-tight top made from a glass cover and PDMS gasket to form a transparent container with cells growing between the cover slip and the agarose. All the components were kept at the target temperature at all times. All experiments were conducted on a Nikon Eclipse Ti microscope fitted with a feedback-controlled heat cage (OkoLab H201 bold line cage incubator), Sutter Instruments Lambda SC shutter and Andor NEO SCC-1758 camera using a Nikon Plan Apo 100X (DIC N2) oil objective, and images acquired using the manufacturer-supplied NIS software.

For each experiment we identified 8-14 isolated single cells on the agar pad, each giving rise to a single colony. Each colony was imaged every 3-4 min in bright field (3.5 V lamp, $\sim$ 60 ms exposure) and every 15 min in YFP fluorescence channel (500 ms exposure). Previous studies have used fluorescence for single-cell segmentation and tracking [1–4]. However, exciting fluorescent markers in cells is known to stress them, so we opted for the less stressing brightfield microscopy. Image segmentation and cell-tracking are performed on brightfield images taken slightly out of focus ($\sim$ half cell diameter) at every time step. We ensured that the resulting cell boundaries are in agreement with in-focus images; fluorescence images are taken in focus.

Mutant: Heat shock stress

Strain and plasmids	Environmental stress	# of independent exp.	# of colonies	# of accepted cells
* MC4100Δ*clpB* w/ClpB-YFP and lacI^q	37 °C	2	10	1756
MC4100Δ*clpB* w/ClpB-YFP and lacI^q	42 °C	2	11	1704

Mutant: Antibiotic stress

Strain and plasmids	Environmental stress	# of independent exp.	# of colonies	# of accepted cells
* MC4100Δ*clpB* w/ClpB-YFP and lacI^q	37 °C + 0.0 µg/mL Km	2	10	1756
MC4100Δ*clpB* w/ClpB-YFP and lacI^q	37 °C + 0.5 µg/mL Km	2	11	1804

Wild-type: Heat shock stress

Strain and plasmids	Environmental stress	# of independent exp.	# of colonies	# of accepted cells
** MC4100 w/lacI^q	37 °C	2	10	2090
MC4100 w/lacI^q	42 °C	2	13	2084

Wild-type: Antibiotic stress

Strain and plasmids	Environmental stress	# of independent exp.	# of colonies	# of accepted cells
** MC4100 w/lacI^q	37 °C + 0.0 µg/mL Km	2	10	2090
MC4100 w/lacI^q	37 °C + 0.5 µg/mL Km	3	16	1948

*This is the same data used for reference in both mutant studies.
**This is the same data used for reference in both wild-type studies.

TABLE S1. Summary of all Experiments Reported in this Study, Related to Experimental Procedures. We simultaneously tracked 8-14 independent and non-interacting colonies in each experiment as described in Supplemental Experimental Procedures, Sec. I.

II. CHEMICALS AND REAGENTS

All reagents were purchased from Sigma-Aldrich except for agarose and IPTG, which was purchased from Serva (Agarose SERVA). Reagents were dissolved in either ethanol (chloramphenicol) or DI water (all other reagents) and filter-sterilized prior to use.

III. STATISTICAL ANALYSIS

III.1. Statistical significance of different doubling times between lineage-groups

Supplementary to Figures 2C and 3A,B and Figures S3C,G,H,M. Since not all lineage-groups exhibit normally distributed doubling times, we used non-parametric statistics, and to furthermore avoid artifacts of low sample sizes, we used both the two-sample Kolmogorov–Smirnov test and the Wilcoxon rank-sum/Mann–Whitney U-test with 5% significance level. As shown by black outline in main Figure 3A,B and Figures S3C,G,H,M, we do observe significant difference for groups which are separated further in the population tree. For groups with little separation, the within-group noise is comparable with the between-group variation. We note that significantly increasing the number of cells in our experiments will lead to statistically significant differences between a larger set of groups, as is illustrated by the extensive data set by Stewart *et al.* [1] (see Figure S2).

III.2. Generating null-distributions for populations of lineage-grouped doubling times

Supplementary to Figures 2D, and 3C,D and S3D,E,I,K N,O. We generated the non-ADS null distributions for the lineage-grouped data sets as follows. Using the unfiltered (including within-group variations) lineage-sorted data, we randomly shuffled two cells between groups and repeated this process 100 times the total number of cells in all groups to get good mixing while preserving the number of cells in each group. After shuffling the median of each group was computed and stored, and the process repeated over 500 times, each time starting from the original, unfiltered lineage-sorted data set. The 500 distributions of medians from each reshuffling process were pooled to generate the presented null distribution. The point of repeating 500 times is to get an idea of how much the data shifts around as a consequence of a reshuffling event, which relates to the variance of the null distribution.

III.3. Investigation of statistically significant difference of population diversities σ

Supplementary to Figures S3A,F,L,P. To test if the population diversities (equivalent to widths of distributions of doubling times), σ, are significantly different at low and high stress we use bootstrapping to estimate the statistical significance of the difference

$$\Delta\sigma = \sigma_{42\ ^\circ\mathrm{C}} - \sigma_{37\ ^\circ\mathrm{C}} \tag{S1}$$

of the population diversities $\sigma_{42\ ^\circ\mathrm{C}}, \sigma_{37\ ^\circ\mathrm{C}}$ at 42 °C and 37 °C respectively. To account for the fact that the associated null distributions change between the two temperatures, see Figure 3C in the main text. we performed the following statistical analysis

- Step (i) perform bootstrapping (random sampling with replacement) on lineage grouped data at 37 °C (using the same number of data points as the original data set) to obtain a value for $\sigma_{37\ ^\circ\mathrm{C}}$.
- Step (ii) perform the same analysis on the lineage-grouped data at 42 °C to obtain a value for $\sigma_{42\ ^\circ\mathrm{C}}$.
- Step (iii) compute $\Delta\sigma$ from Eq. (S1).
- Step (vi) repeat steps $(i) - (iii)$ 10^4 times to obtain distribution of differences $\Delta\sigma_{\mathrm{LS}}$.
- Step (v) repeat steps $(i) - (iv)$ using the associated null-distribution data instead of the lineage-grouped data at each temperature to obtain distribution of differences $\Delta\sigma_{\mathrm{null}}$.

The null-distribution difference $\Delta\sigma_{\mathrm{null}}$ reflects the variation in sample-size in lineage groups between the two temperatures. The population diversities at low and high stress are statistically significantly different, if the distribution of actual differences $\Delta\sigma_{\mathrm{LS}}$ is significantly different from the distribution of differences in corresponding null distributions$\Delta\sigma_{\mathrm{null}}$. This is indeed the case as shown in Figure S3A,F,L,P. The distributions under all stresses are significantly different ($P<0.01$, two-sample t-test analysis). Thus the population diversity σ increase significantly under heat and kanamycin stress in both wild-type (MC4100) and MC4100ΔClpB+ ClpB-YFP strains.

III.4. Aggregate data statistics

Supplementary to Figures 4 and S4. At any pole age, the aggregate data follows a binomial distribution with an age-specific probability p_a of having an aggregate. For the case with N^a_{agg} aggregates and N^a_{cells} cells we compute

the frequency (estimated probability) of aggregates $f_a = \frac{N^a_{\text{agg}}}{N^a_{\text{cells}}}$, and the standard deviation of the frequency $\sigma_{f_a} = \sqrt{\frac{f_a(1-f_a)}{N_{\text{cells}}}}$ using the standard formulae for the binomial distribution.

III.5. Standard error of the mean for populations of cells

Supplementary to Figures 5A and S5D. Distributions of single-cell doubling times were not normal, so we used bootstrapping to obtain standard error of the mean (SEM): we resampled the data with replacement to obtain a single realization of the population mean, and repeat a total of 10^4 times, thereby producing a distribution of means. This resulting distribution of means follows a normal distribution and is thus well-characterized by its standard deviation, which is the SEM.

III.6. Difference of doubling times ΔT of damage accumulating/evading lineages

Supplementary to Figure 5A, S5A and S5D. In Figures 5A and S5D we show the difference in doubling times between the consecutively damage-accumulating and consecutively damage-evading lineages (corresponding to all-green and all-magenta lineages in Figure 2A) originating from the same ancestor. We always start from an ancestor which has once undergone damage-evading event and at each generation record doubling times of consecutively damage-accumulating cells. This produces a sequence of doubling times $T_{\text{accum}}(n)$ as a function of generation number n following the initial cell for damage-accumulating. Repeating the analysis for the consecutively damage-evading lineage produces the sequence T_{evad}. The difference ΔT is at each generation n the difference between the two sequences, $\Delta T(n) = T_{\text{accum}}(n) - T_{\text{evad}}(n)$.

The repeats in the experimental data are averaged at each generation n before subtracting; we use the $\overline{\ }$ to denote average within each generation of such a lineage, our experimental results are expressed as $\Delta\overline{T}(n) = \overline{T}_{\text{accum}}(n) - \overline{T}_{\text{evad}}(n)$.

III.6.1. Analytical expression

Experimentally, cells were grown at some temperature for ~ 24 h prior to the start of an experiment, and they have therefore adapted to this state. Since the state of the initial cell in an experiment is unknown, we take it to be the average $\langle D\rangle$. Since $\langle D\rangle$ scales linearly with λ we will also write $\lambda\langle\tilde{D}\rangle = \langle D\rangle$. Damage-accumulating lineages inherit the fraction $(1+a)/2$ of ancestor damage, while damage-evading inherit $(1-a)/2$ of ancestor damage.

Starting from the average damage $\langle D\rangle$, the damage in the damage-accumulating sibling in the first few generations is

$$\begin{aligned}
&\text{Gen. 0}: \quad \lambda\langle\tilde{D}\rangle,\\
&\text{Gen. 1}: \quad \lambda\left[1+\frac{1+a}{2}\langle\tilde{D}\rangle\right],\\
&\text{Gen. 2}: \quad \lambda\left[1+\frac{1+a}{2}\left[1+\frac{1+a}{2}\langle\tilde{D}\rangle\right]\right] = \lambda\left[1+\frac{1+a}{2}+\left(\frac{1+a}{2}\right)^2\langle\tilde{D}\rangle\right],
\end{aligned} \tag{S2}$$

Thus, the damage in the consecutive old-pole lineage at generation q after the common ancestor is given by

$$H_{\text{old}}(q) = \lambda\left[\sum_{i=0}^{q-1}\left(\frac{1+a}{2}\right)^i + \left(\frac{1+a}{2}\right)^q\langle\tilde{D}\rangle\right] \text{ for } q>0,$$

Similarly, we find for the new-pole history starting from average damage $\langle D\rangle$

$$H_{\text{new}}(q) = \lambda\left[\sum_{i=0}^{q-1}\left(\frac{1-a}{2}\right)^i + \left(\frac{1-a}{2}\right)^q\langle\tilde{D}\rangle\right] \text{ for } q>0.$$

The difference $\Delta T(q)$ of doubling time histories (old pole minus new pole) at generation q following the common ancestor is therefore given by

$$\begin{aligned}\Delta T(q) &= t_{\min} + \mu H_{\text{old}}(q) - [t_{\min} + \mu H_{\text{new}}(q)] \\ &= \mu\lambda\left(\left[\sum_{i=0}^{q-1}\left(\frac{1+a}{2}\right)^i + \left(\frac{1+a}{2}\right)^q \langle\tilde{D}\rangle\right] - \left[\sum_{i=0}^{q-1}\left(\frac{1-a}{2}\right)^i + \left(\frac{1-a}{2}\right)^q \langle\tilde{D}\rangle\right]\right),\end{aligned} \tag{S3}$$

which holds for $q > 0$.

This formula (Eq. (S3)) was fitted to the experimental data in Figure 5A and S5D.

III.6.2. Linear scaling of $\Delta T(n)$ under different stresses

Equation S3 predicts that the difference $\Delta T(n)$ will follow almost the same functional form under different stresses, since the stress-dependence of $\langle D\rangle$ is secondary compared to the linear dependence of the prefactor. Higher stresses (larger λ) shift the the curve up, so plotting against each other $\Delta T(n)$ under two different stresses 1 and 2, the slope α of the curve will be well approximated by the ratio of their stress levels $\alpha = \lambda_2/\lambda_1$. This prediction is confirmed from our experimental data in Figure S5A.

III.7. Fitting population model to experimental data for the doubling-time difference of damage-accumulating/evading lineages $\Delta\overline{T} = \overline{T}_{\text{accum}} - \overline{T}_{\text{evad}}$

We fit our population model using both constant asymmetry and damage-dependent asymmetry to the experimental population data for the difference of doubling times of the damage-accumulating/evading lineages. For the analytical model we use Eq. (S3), while we rely on simulations for the model with damage-dependent asymmetry.

We fit simultaneously to the data under low and high stress, because both can be used to infer system-specific parameter values, while each independently can be used to infer the specific stress-level. These fits serve the dual purpose of (*i*) determining which of the two models best describe the data (i.e. as a test of whether damage-dependent asymmetry indeed is detectable at the population level), and (*ii*) determine the remaining free model parameters μ, and λ under both low and high stress, henceforth denoted λ_{L} and λ_{H}. The minimum doubling time $t_{\min}$ is not know directly from our measurements, and the difference of doubling times $\Delta T(n)$ depends only very weakly on the exact value (tested the plausible range $t_{\min} \in [15; 30]$ min). We set $t_{\min} = 22$ min (corresponding to the low stress conditions in our data) in all fitting procedures.

We have fitted the experimental data using the analytical model with the value $a = c_1 = 0.7411$ obtained above from the aggregate inheritance data (see Table S2), the theoretical optimum at $a = 1$, and using damage-dependent asymmetry with parameters from Table S2. We find that model with damage-dependent asymmetry is by far superior, indicating that experiments support only $a(D)$ (Akaike weight $w \approx 0.99$) and exclude models with constant asymmetry.

III.8. Analyses of the damage-dependent asymmetry

Using the experimental data on aggregate area asymmetry at cell division (Figure S5B), we can estimate the asymmetry function $a = a(D)$ that this data implies, see Figure S5C. The asymmetry is clearly not constant, but has sigmoidal dependence on aggregate area. Sigmoidal functions assures that asymmetry will lie between physiologically plausible values 0 and 1. We find that the best fitting function is $a = \frac{c_1 + D^{c_3}}{c_2 + D^{c_3}}$, with parameters shown in Figure S5C. The parameter values obtained from least-squares fitting.

III.9. Calculation of AIC_{c} values in the Akaike Information Criterion

Formally, the value of AIC_{c} is given by

$$\text{AIC}_{\text{c}} = -2\log\left(\mathcal{L}(\hat{\theta}|y)\right) + 2K + \frac{2K(K+1)}{n-K-1}, \tag{S4}$$

where $\hat{\theta}$ is a vector containing the model parameters (the model-specific c_i's and the unknown "noise" variance σ of the residuals) maximizing the likelihood function given the experimental data y, $\mathcal{L}$ is the maximized likelihood

Condition	Model	λ_L [μm^2] (37C, no KM)	λ_H [μm^2]	μ [min μm^{-2}]	χ^2_{red}	Akaike weight, w
MC4100ΔclpB	Const. asym. $a = 0.7411$	0.1330	0.4797	3.9723	12.7834	1.098×10^{-3}
Heat stress	Const. asym. $a = 1$	0.1042	0.3779	3.1468	12.2756	9.3149×10^{-3}
	Dam. dep. asym.	**0.0869**	**0.1610**	**12.8364**	**4.0668**	**0.9896**
MC4100ΔclpB	Const. asym. $a = 0.7411$		0.3001		9.0944	2.3674×10^{-4}
Kanamycin stress	Const. asym. $a = 1$	same as above	0.2294	same as above	6.9103	4.3942×10^{-3}
	Dam. dep. asym.		**0.1228**		**3.3245**	**0.9954**
MC4100	Const. asym. $a = 0.7411$	0.1995	0.3343	3.5126	5.1804	8.955×10^{-5}
Kanamycin stress	Const. asym. $a = 1$	0.1484	0.2648	2.7448	3.8387	1.9786×10^{-3}
	Dam. dep. asym.	**0.1188**	**0.1693**	**6.9518**	**1.2389**	**0.9979**
MC4100	Const. asym. $a = 0.7411$		0.2418		4.2229	1.457×10^{-4}
Heat stress	Const. asym. $a = 1$	same as above	0.1905	same as above	3.0803	3.290×10^{-3}
	Dam. dep. asym.		**0.1417**		**1.0000**	**0.9966**

TABLE S2. Supporting table for Figure 5A and Figure S5 showing best-fit parameters λ_L, λ_H and μ for the three models: "Const. asym. $a = 0.7411$", "Const. asym. $a = 1$" and "Dam. dep. asym." with $t_{min} = 22$ min. The low-stress parameter, λ_L, corresponds to the condition of 37C and no Kanamycin, thus we use same values of λ_L for the same strain. Stress parameter is expressed in units of aggregate size. Last two columns show the goodness of the fit: the reduced χ^2-values (χ^2_{red}) for each model indicating how well it fits the experimental data relative to the uncertainty of the experimental measurement and the Akaike weights w which estimates the relative level of support in favor of each model best describing the data relative to the two other models. The best model (highlighted in boldface) is damage-dependent asymmetry according to the Akaike weights, while the two other models are doing substantially worse. The residuals of this best model is on par with the measurement error and are consequently as good as can be expected.

function (likelihood function evaluated at its maximum point, i.e. at the parameter values $\hat{\theta}$) of the model given the experimental data y, n is the sample size and K is the number of free parameters in the model together with the unknown noise variance of the residuals (that is, $K = \tilde{K} + 1$ where $\tilde{K}$ is the number of free parameters in the model, e.g. the number of c_is). The last term on the right hand side of this equation is the second-order correction term needed to provide better estimates at small sample sizes.

We used least-squares fitting to obtain the optimal parameters. For our models, the least-squares optimal parameters are related to the maximum-likelihood optimal parameters through a simple relationship, assuming the residuals follow a normal distribution [5]. This relationship stipulates

$$\log\Big(\mathcal{L}(\hat{\theta}|y)\Big) \approx -\frac{n}{2}\log\hat{\sigma}^2 \tag{S5}$$

where $\hat{\sigma}^2 = \sum_i \epsilon_i^2/n$ is given in terms of the squared residuals ϵ_i from the least-squares fit and the number of samples n. The approximation in Eq. (S5) consists of dropping constant terms which are the same for all models, which become irrelevant since only the differences in AIC_c values between models is of importance. We therefore replace Eq. (S4) by

$$AIC_c = n\log\left(\hat{\sigma}^2\right) + 2K + \frac{2K(K+1)}{n-K-1}, \tag{S6}$$

and use this to compute the AIC_c values. We have checked that using actual maximum likelihood estimation provides numerically indentical results for the c_i's, Δ and w for all three models, with irrelevant differences in raw AIC_c values between the two approaches a consequence of the approximation in Eq. (S5).

III.10. Quantification of the ADS-unrelated cell-to-cell variation

The statistical similarity of the within-age-group noise at each temperature allowed us to pool all noise from each age group. Interestingly, the resulting distributions, given as full lines in Figure S5, appear fairly similar. However, the fold-increase in noise distribution width σ^n is 1.37 between the two temperatures ($\sigma^n_{37\,^\circ C} = 4.97$ min and $\sigma^n_{42\,^\circ C} = 6.79$ min). For comparison the fold-increase in the width σ^{LS} of the distribution of lineage-sorted data is 1.93 ($\sigma^{LS}_{37\,^\circ C} = 1.06$ min and $\sigma^{LS}_{42\,^\circ C} = 2.05$ min). To take into account the difference in means, we computed the coefficient-of-variance of population doubling times $\tilde{C} = \sigma/\langle T\rangle$ for lineage-sorted data and noise (in both cases normalizing the population-mean) at the two stress levels, and found that while the parameter does increase for

the noise distributions by a factor 1.28 (from $\tilde{C} = 0.18$ to $\tilde{C} = 0.23$) this increase is larger for the lineage-sorted data (increase by a factor 1.8; from $\tilde{C} = 0.04$ to $\tilde{C} = 0.07$). These results are conistenet across all the strains and conditions. It follows that the variations of width of whole-population-distributions of doubling times in response to increasing stress are caused primarily by asymmetric damage segregation, and are only secondarily a consequence of noise increasing in response to stress as well.

IV. AGENT-BASED NUMERICAL SIMULATIONS

The models have been implemented in MATLAB R2012b. In all reported cases we have started the simulations from a single cell with 0 inherited damage. MATLAB code for both models will be made available per request.

To simulate the growing population, we first construct the entire population tree for a specified number of generations. Next for each cell in the tree we compute and record cell's damage and doubling time as given in Eq. 1 and 2 in the main text. To extract population quantities such as population-average doubling time, population-distribution of damage etc., we make a second sweep through the population tree and query for any property of interest. Up to ~ 30 generations of cell divisions can be simulated on a laptop within reasonable time (yielding about 10^9 cells).

Since the cells divide a deterministic time $t_{\min} + \mu D$ following last division, and the simulations start from a single cell, there is a transient period when cells are synchronously divide at the same time. After about 10 generations the divisions are slowly desynchronized. The synchronous divisions affect the sampling of distributions of doubling times (one has to go beyond 30 generations to reach steady state distributions) and to avoid it we add small-amplitude zero-mean noise to $t_{\min}$ for 5 consecutive generations to all cells present, starting at generation 5. The amplitude of this noise is $\mu\lambda/5$ but seems to be largely irrelevant within reasonable ranges. By this process we can thus reach a faster convergence of the damage distribution without affecting the population growth rate. This approach is valid as real doubling times are also noisy (see Figure S5E).

IV.1. Simulations with physiological levels of noise, Figure 6A

For these simulationsthe noise is added on the ADS-unrelated minimum generation time $t_{\min}$, by adding a random number ξ to $t_{\min}$ for each cell, with ξ taken from the experimentally determined zero-mean distribution of physiological noise 42 °C shown Figure S5E.

IV.2. Mean and standard deviation of population-distribution of doubling times, Figure 1A-C and 6A

At each time point in the simulations we obtain the instantaneous means of damage $\overline{D}(t)$ and doubling time $\overline{T}(t)$ and width $\sqrt{\overline{T^2} - \overline{T}^2}$ of the population-distribution of doubling time. We store all values starting at $t = 20 \times (t_{\min} + \mu\lambda)$, and for each statistic $\overline{D}(t)$, $\overline{T}(t)$ or $\sqrt{\overline{T^2} - \overline{T}^2}$ obtain a mean and a standard deviation over the storage interval which we use for the true population-averaged values of these statistics $\langle D \rangle$, $\langle T \rangle$ and σ. For each statistic we also estimate and show the variations (standard deviation) across the sampling interval. Results using this approach are given in Figure 1B,C,E.

V. THEORETICAL MODEL

Here we sketche out an overall description of our analytical approach and present the final formulae. The details of model derivation will be published elsewhere.

The whole-population effects of ADS can be analyzed analytically by mapping the problem of ADS to the Ising model in physics[6]. This enables us to relate microscopic details of interactions between ancestral and current cells to the macroscopic observables on the population level, e.g. growth rate and damage distribution among cells. The Ising model describes the behavior of a system of interacting physical particles. Each system state is a specific combination of individual particle states. The particle states are binary (denoted by ± 1 and often referred to as spin up and spin down states), and the probability that a particle occupies a given state is affected by the states of the nearest-neighbor particles. In the one-dimensional case, this corresponds to a linear chain of particles, known as an Ising chain.

Here, we map each lineage in a growing bacterial population onto a unique system state of an Ising chain. A lineage encompasses all known ancestors of a given cell, and every lineage begins with the first cell in the bacterial colony.

Two examples of lineages are highlighted by the green and magenta lines in Figure 1A. The state (± 1) of a single cell within a lineage dictates the amount of damage inherited from its ancestor, preserving the concept of nearest-neighbor interactions. By relating damage inheritance to the division time of a cell (Eq. 2), we find that the sequence of cell states (± 1) within a lineage determines the total time elapsed from the first cell to the most recent division in the lineage. Thus, the time spanned by a lineage is analogous to the energy of a specific Ising chain configuration. The goal is to determine the statistical properties of a bacterial population at time t, which is equivalent to the statistical properties across many Ising chains with fixed system energy E. Thus, by this analogy, statistical moments such as the mean and standard deviation (population width) of e.g. doubling times across the biological population of cells can be computed using the ensemble averages of the equivalent model in statistical physics. This method allows us to derive approximate analytical expressions for the mean doubling time $\langle T \rangle$ and the width σ of the distribution of doubling times.

V.1. Mean and variance of population damage and doubling time

Using these approach we find the following approximate result for the mean doubling time

$$\langle T \rangle \approx t_{\min} + \mu\lambda \left[2 + a^2 \lambda\mu\beta\varepsilon^* \frac{(27\beta\varepsilon^*\lambda\mu - 2)a^2 - 18}{8} \right] \quad . \tag{S7}$$

We furthermore find for the width of the population-distribution of doubling times

$$\sigma \approx \frac{\mu\lambda a}{4} \sqrt{20 + a^2 \left[4 + \beta\varepsilon^*\lambda\mu \left(-44 - 45\beta\varepsilon^*\lambda\mu + a^2 \left\{ 2 + 9\beta\varepsilon^*\lambda\mu \left[1 + \beta\varepsilon^*\lambda\mu \left(27 + a^2 \left\{ 2 - 18\beta\varepsilon^*\lambda\mu \right\} \right) \right] \right\} \right) \right]} \tag{S8}$$

where $\beta\varepsilon^* = \frac{8\lambda\mu + 4t_{\min} - 2f(a,\lambda,\mu,t_{\min})}{a^2(9+2a^2)\lambda^2\mu^2}$ and $f(a,\lambda,\mu,t_{\min}) = \sqrt{2}\sqrt{8\lambda\mu t_{\min} + 2t_{\min}^2 - \lambda^2\mu^2\left[9a^2\ln 2 - 8 + a^4 \ln 4\right]}$. In these expressions, a is the asymmetry parameter, $t_{\min}$ is the minimum damage-independent single-cell doubling time, λ is the amount of acquired environmental damage per generation, and μ is the conversion factor between damage and doubling time. All expressions have been derived assuming $a > 0$.

The two results from Eqs. (S7) and (S8) are given in Figure 1B and E in the main text. We find good agreement with simulation results throughout, except for the width σ for a close to 1 when $\lambda\mu$ is large ($\lambda\mu > 1$), where Eq. (S8) slightly overshoots.

V.2. Special case of symmetric division, $a = 0$

The special case of symmetric division ($a = 0$) is not handled by our approximate analytical expressions, however, in this special case all cells carrying the same amount of damage and divide and average population-properties are identical to single-cell properties; thus, we can easily provide exact analytical expressions for the population behavior.

Inheriting exactly 50 % of the ancestor's damage, the damage in generation n of a single cell starting from 0 damage at the first generation and acquiring λ damage from the environment in each generation, is given by $D(n) = \lambda \sum_{j=1}^{n} \frac{1}{2^{j-1}}$. For large n, this damage stabilizes to a constant level $D(n) = 2\lambda$ because the geometric series $\sum_{j=1}^{n} 1/2^{j-1}$ converges to 2 for $n \to \infty$. In this long-time limit, all cells in the population have the same amount of damage, and so it follows directly that $\langle D \rangle = 2\lambda$ and $\sigma_D = \sqrt{\langle D(n)^2 \rangle - \langle D(n) \rangle^2} = 0$. From the relationship between damage and doubling time Eq. (2) in the main text, we find for the distribution of doubling times

$$\langle T \rangle = t_{\min} + \mu \langle D \rangle = t_{\min} + 2\mu\lambda \quad \text{and} \quad \sigma = \mu\sigma_D = 0. \tag{S9}$$

[1] E. J. Stewart, R. Madden, G. Paul, and F. Taddei, PLoS Biology **3**, e45 (2005).
[2] A. B. Lindner, R. Madden, A. Demarez, E. J. Stewart, and F. Taddei, Proc. Nat. Acad. Sci. USA **105**, 3076 (2008).
[3] P. Wang, L. Robert, J. Pelletier, W. L. Dang, F. Taddei, A. Wright, and S. Jun, Curr. Biol. **20**, 1099 (2010).
[4] J. Winkler, A. Seybert, L. König, S. Pruggnaller, U. Haselmann, V. Sourjik, M. Weiss, A. S. Frangakis, A. Mogk, and B. Bukau, EMBO Journal **29**, 910 (2010).
[5] K. P. Burnham and D. R. Anderson, *Model selection and multimodel inference: a practical information-theoretic approach*, 2nd ed. (Springer, 2002).
[6] R. J. Baxter, *Exactly solved models in statistical physics* (Academic Press, 1982).

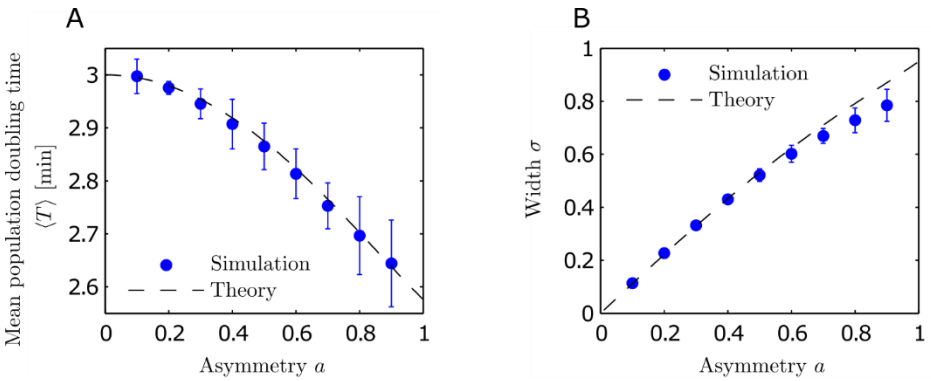

Figure S1. Effects of Asymmetry a on Model Predictions, Related to Figure 1. Errorbars on simulation results indicate standard deviations on the presented metrics. These arise as a consequence of using a stochastic simulation algorithm. **A.** Mean doubling time $\langle T \rangle$ decreases with asymmetry a. Theoretical results computed from Eq. S30. **B.** Width of population-distribution of doubling times σ increases with a, with theoretical prediction given in Eq. S8. Results shown are for the model where all cells have the same asymmetry parameter, t_{min} = 1 min, $\lambda = 1\mu^2$ and $\mu = 1$ min μ^{-2}. Details of theoretical calculations and agent-based simulations are given in Supplemental Experimental Procedures, Sections IV and V.

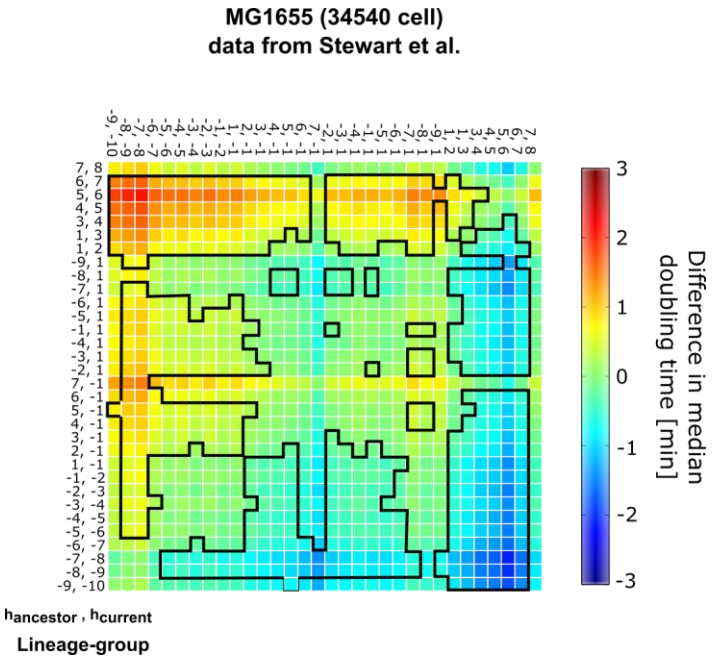

Figure S2. Validation of Lineage-Based Analyses Using Data from Stewart et al.[1], related to Figure 2 **A.** Heatmap of the pairwise differences in median doubling times for each pair of lineage-groups, with notations as in main Figure 2C. Each colored square in the heat map color-codes the difference between the corresponding vertical and horizontal lineage-groups. Significant differences are outlined in black. Statistical significance was computed using the non-parametric Wilcoxon rank-sum test (Mann-Whitney U-test) at the 5% significance level. Similar results are obtained with non-parametric two-sample Kolmogorov-Smirnov test.

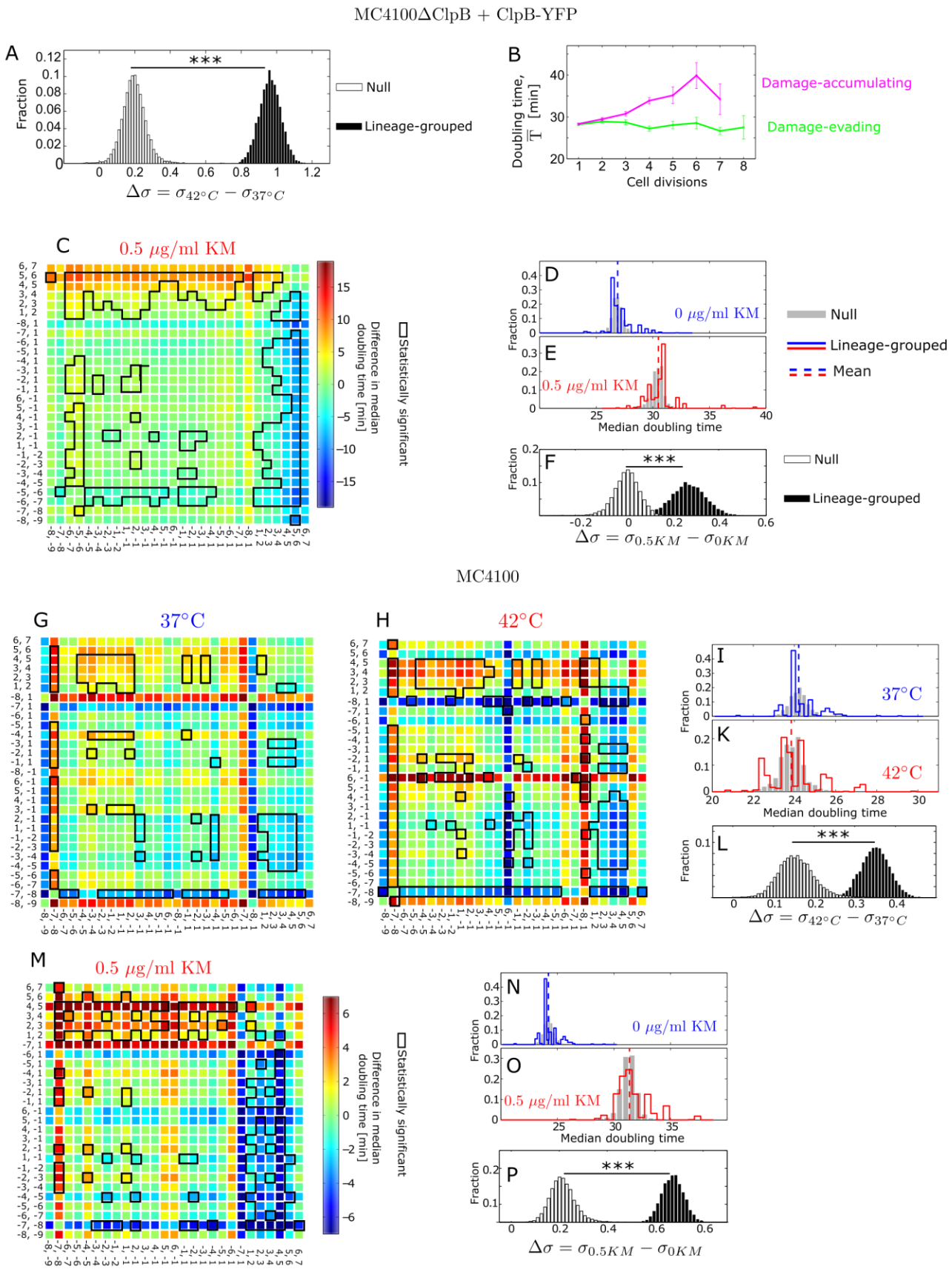

Figure S3. ADS Quantification across Strains and Stresses, Related to Figure 3.
A. The distributions of the differences $\Delta\sigma$ used to statistically test the increase in population

diversity, σ, under heat stress (for data presented in Figure~3C,D). The distributions are obtained as described in Supplemental Experimental Procedures, Sec.III.3. The differences are calculated independently for the lineage-grouped data (filled bars) and the associated null-distribution data (open bars). The population diversity at 42℃, $\sigma_{42℃}$, is statistically significantly different from the population diversity at 37℃, $\sigma_{42℃}$. *** denotes statistically significant difference (P<0.01, by two-sample *t*-test analysis). **B.** Doubling times of lineage-groups with successive rounds of damage-accumulation (or damage-evasion) converge to steady values. We plot the experimentally obtained doubling times of the consecutive old-pole lineage (magenta) and new-pole lineage (green) as a function of the number of generations from the initial cell. Errorbars mark standard error of the mean obtained via bootstrapping.

C. Heatmap, obtained as in Figure 2C, for population of MC4100ΔclpB + ClpB-YFP cells stressed by 0.5 μg/ml kanamycin. The heatmap for unstressed cells is shown in main Figure 3A.

D-E. Distributions of doubling times, obtained as in Figure 2D, for populations of MC4100ΔclpB + ClpB-YFP cells that were either not stressed (blue) or kanamycin-stressed (red).

F. The distributions of the differences $\Delta\sigma$, obtained as in A. and used to statistically test the increase in population diversity, σ, under kanamycin stress for MC4100ΔclpB + ClpB-YFP population.

G-H. Heatmaps, obtained as in Figure 2C, for populations of wild-type (MC4100) cells at 37℃ and heat-stressed at 42℃. The colorbar is the same as in **M.**

I-K. Distributions of doubling times, obtained as in Figure 2D, for populations of wild-type cells at 37℃ (blue) and heat-stressed at 42℃(red).

L. The distributions of the differences $\Delta\sigma$, obtained as in A. and used to statistically test the increase in population diversity, σ, under heat stress.

M-P. Figures corresponding to H-L, but in response to kanamycin stress.

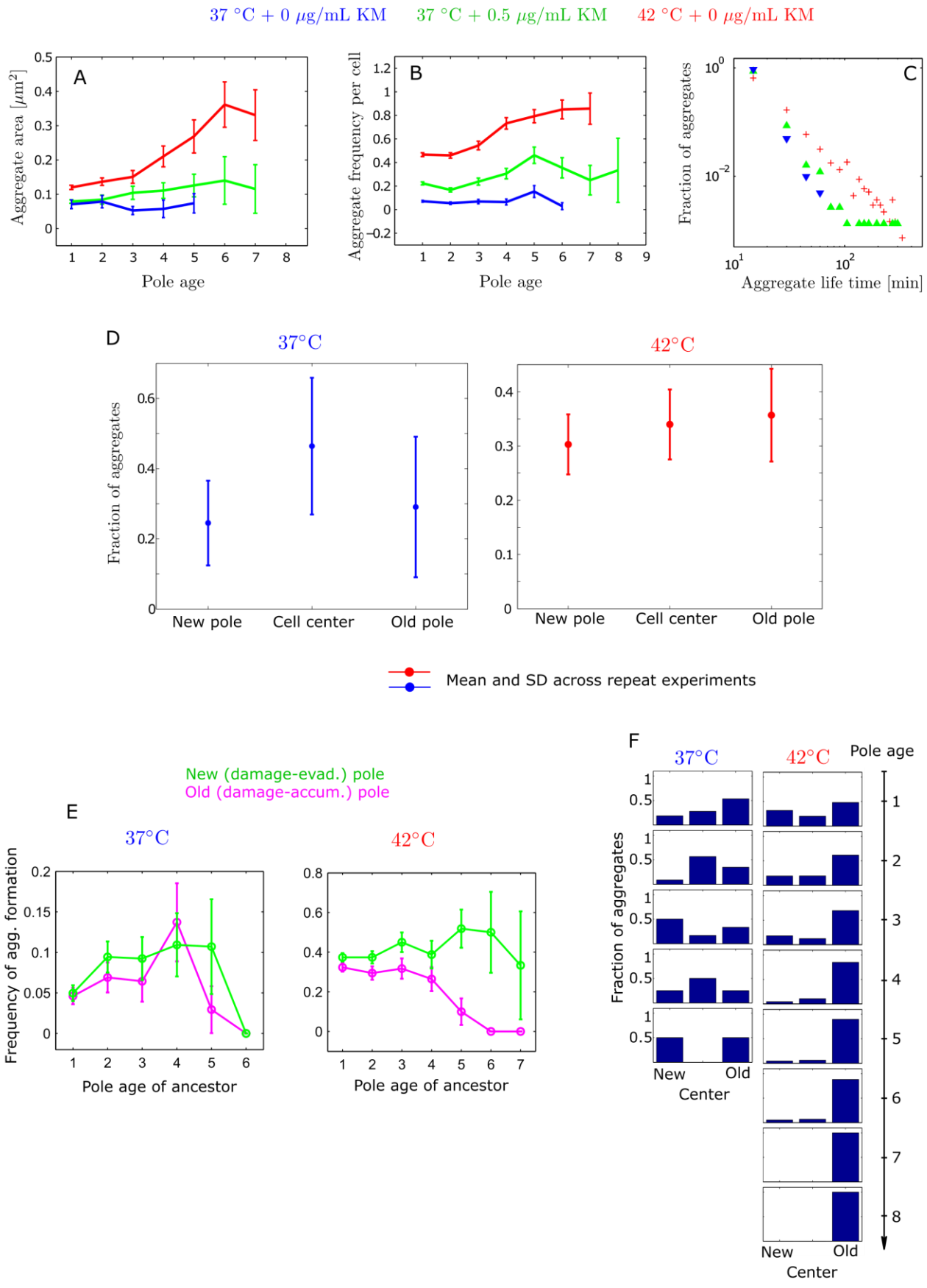
37 °C + 0 μg/mL KM
37 °C + 0.5 μg/mL KM
42 °C + 0 μg/mL KM
A
Aggregate area [μm²]
Pole age
B
Aggregate frequency per cell
Pole age
C
Fraction of aggregates
Aggregate life time [min]
D
37°C
42°C
Fraction of aggregates
New pole
Cell center
Old pole
Mean and SD across repeat experiments
E
New (damage-evad.) pole
Old (damage-accum.) pole
37°C
42°C
Frequency of agg. formation
Pole age of ancestor
F
37°C
42°C
Pole age
Fraction of aggregates
New
Old
Center

Figure S4. Dynamics of Protein Aggregates Provides Mechanistic Explanation of Stress-Induced ADS, Related to Figure 4.

A. Aggregate size increases with pole age and under stress. This confirms the model assumption that damage gradually increases through the old-pole lineage. Errorbars indicate 95% confidence interval.

B. Supporting figure to main Figure 4E, showing the frequency of aggregates in kanamycin-stressed cells. Errorbars indicate standard deviation (see Methods).

C. Supporting figure to main Figure 4C, showing the stability of aggregates in kanamycin-stressed cells.

D. Aggregates are equally likely to form in any of the three regions of the cell. Dots mark the mean over all colonies and errorbars represent standard deviation, quantifying colony-colony variations.

E. Frequency of formation of new aggregates for sister cells as a function of the pole-age of their common ancestor. Frequency at 37℃ and 42℃ is nominally constant, except for old-pole cells at 42℃ where we observe a decrease for older pole ages, corresponding to the increasing frequency of inheritance f^{inh} seen in the main Figure 5B. Errorbars indicate standard deviation (see Methods).

F. Fraction of all aggregates found in the three intracellular regions at each pole age. Aggregates passively move to the old pole after a few divisions when aggregate inheritance is prevalent (42℃) but cannot do this when the aggregates are short-lived and the inheritance is thus insignificant (37℃). This confirms the earlier observations by Lindner *et al.* [2].

All data is sampled in the mutant strain MC4100ΔclpB + ClpB-YFP.

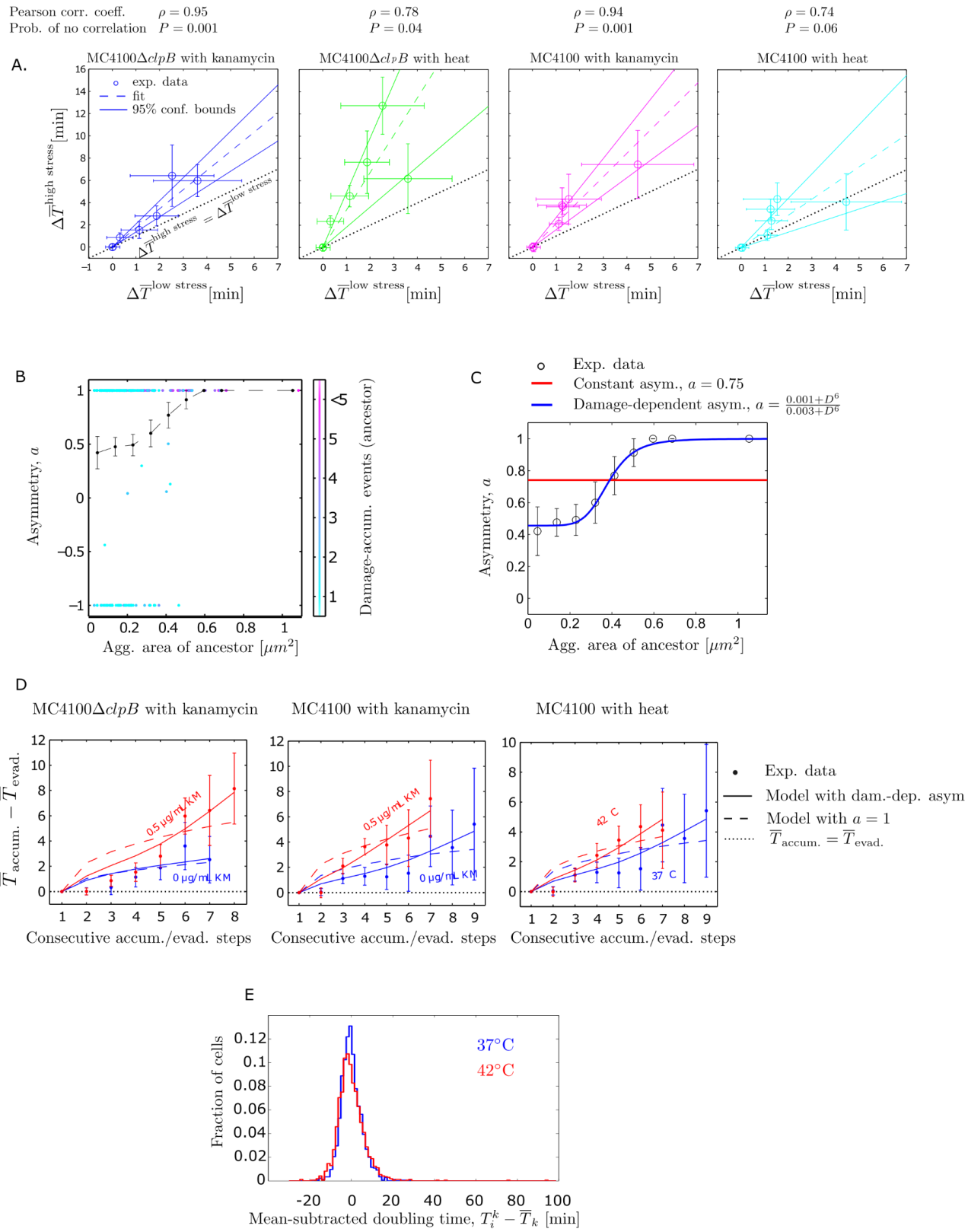

Figure S5. Model Validation Steps, Related to Figure 5.

A. Model and data agree on the near-linear correlation between mean doubling time difference of

consecutive damage accumulating/evading lineages under low and high stress ($\Delta\bar{T}^{high\ stress} \propto \Delta\bar{T}^{low\ stress}$, see Sec. III.6). Circles are the means and errorbars are the standard error of the means. Dashed lines are the error-weighted best fits and full lines are 95% confidence interval.
Pearson linear correlation coefficient ρ and the associated probabilities P of having a similar value of ρ under the null hypothesis of no correlation between the low-stress and high-stress data indicate statistically significant (positive) linear correlation between low-stress and high-stress conditions across all investigated strains and stresses at the 5 % level.
B. Supplementary figure to main Figure 5C. Experimental measurements of average asymmetry $\langle a \rangle = \frac{A_{OP}^{inh} - A_{NP}^{inh}}{A_{OP}^{inh} + A_{NP}^{inh}}$, where A_{OP}^{inh} and A_{NP}^{inh} is the total are of inherited aggregates to the old-pole and new-pole offspring, respectively.
C. Lines show the best fits of the models with constant (red) and damage-dependent (blue) asymmetry.
B.-C. Errorbars mark standard deviation.
D. Supplemental to main Figure 5A. Difference $\Delta\bar{T}$ of doubling times of extreme-branch lineages in the population tree for both low (blue) and high stress (red) obtained from experimental data (filled circles). The parameters inferred from model fits are summarized in Table S2. Dashed lines give result using model with constant asymmetry ($a = 1$) while full lines shows a superior result from model with damage-dependent asymmetry.
E. Quantification of ADS-unrelated noise through the distribution of ``centered" doubling times (for MC4100ΔclpB). For each cell, the mean of the lineage-group is subtracted from the measured doubling time: $\tilde{T}_i^k = T_i^k - \bar{T}^k$, where T_i^k is the doubling time of cell i in lineage group k and $\bar{T}^k$ is the mean doubling time in lineage group k.